AGU100 ADVANCING EARTH AND SPACE SCIENCE

JGR Solid Earth

RESEARCH ARTICLE
10.1029/2019JB018386

Key Points:
- The near-field velocity pulse brought from the 2002 Denali earthquake brought the uppermost 2 km beneath Pump Station 10 into failure
- High-frequency *S* waves passing through the failed zone were strongly attenuated
- Non-linear failure also occurred within gravel in the uppermost 100 m beneath Pump Station 10

Correspondence to:
N. H. Sleep,
norm@stanford.edu

Citation:
Sleep, N. H., & Liu, T. (2020). Nonlinear Suppression of High-Frequency *S* Waves by the Near-Field Velocity Pulse With Reference to the 2002 Denali Earthquake. *Journal of Geophysical Research: Solid Earth*, *125*, e2019JB018386. https://doi.org/10.1029/2019JB018386

Received 15 JUL 2019
Accepted 26 OCT 2019
Accepted article online 7 NOV 2019

Nonlinear Suppression of High-Frequency *S* Waves by the Near-Field Velocity Pulse With Reference to the 2002 Denali Earthquake

Norman H. Sleep[1] and Tianze Liu[1]

[1]Department of Geophysics, Stanford University, Stanford, CA, USA

The near-field velocity pulse of large strike-slip earthquakes brings near-fault stiff crystalline rock into failure. The uppermost ~2 km beneath Pump Station 10 (PS10) likely failed nonlinearly during the 2002 Denali earthquake. High-frequency *S* waves traversed this region during and immediately after failure with only weak waves reaching the surface. In contrast, high-frequency *S* waves were briefly weak at station LUC only during the strong near-field velocity pulse of the 1992 Landers earthquake. The observed horizontal spectra during the near-field velocity pulse at PS10 decreased exponentially with frequency with a low apparently constant *Q* of ~20. This observation is incompatible with simple elastic-plastic and nonlinear viscoelastic rheologies that do not preferentially attenuate high frequencies. Candidate rheologies involve heterogeneous crystalline rock masses where nonlinear domains act in parallel. Maxwell (spring and dash pot) elements in parallel produce apparently constant *Q* over a range of frequencies. This rheology may arise from pseudolinear inelastic interaction of weak stresses from high-frequency *S* waves with strong low-frequency stresses from the near-field velocity pulse. Alternatively, inelastic deformation associated with the high-frequency waves may interact nonlinearly with low-frequency deformation associated with healing of damage associated with the near-field velocity pulse. The latter process is attractive for the PS10 signal which remained weak after the near-field velocity pulse had passed. We unsuccessfully examined aftershock records for healing of damage within the uppermost crystalline rock.

1. Introduction

Rupture during major earthquakes on strike-slip faults propagates laterally to the first order, as the depth of the seismogenic zone is much less than the length of rupture. The near-field velocity pulse propagates at essentially the rupture velocity. High stresses near the rupture tip drive further rupture. In addition, high stresses cause failure in the near-fault environment at depth and failure at shallower depths farther from the fault (Figure 1). A flower structure of damaged rock develops near frequently active faults (e.g., Ma & Andrews, 2010).

"Inelastic" (or "anelastic") strain from strong dynamic stresses within the flower structure dissipates energy from the near-field velocity pulse. The net effect is nonlinear attenuation (Roten et al., 2014, 2016; Roten, Olsen, Cui, & Day, 2017). The shaking at the surface for a given fault motion history is systematically less than it would have been had the Earth behaved elastically. In addition, the attenuation suppresses energy that would have otherwise driven rupture often making the earthquake smaller than one in an elastic medium with given fault properties and given prequake stress field. In particular, shallow nonlinear attenuation suppresses waves at shallow (uppermost kilometers) depths causing the shallow slip to be systematically less than the slip at ~5 km depth (Kaneko & Fialko, 2011; Roten, Olsen, & Day, 2017).

The purpose of this paper is to empirically examine near-fault failure from the near-field velocity pulse with attention to the uppermost kilometers and failure within crystalline rock. We consider a process envisioned by Sleep and Nakata (2015). Rocks respond to the stress tensors, and strain tensors imposed collectively by seismic waves and do not distinguish between different types of seismic waves. In this paper, high-frequency *S* waves propagate through the moderately shallow region (uppermost ~2 km), while the near-field velocity pulse causes dynamic failure.

We use this partition of wave categories for convenience of discussion. Our signal is broadband, and the transition from low (<1 Hz) to high frequency (~10 Hz) signal is gradational. To inflict some semantics, we use the term "near-field velocity pulse" in a phenomenological or engineering sense (e.g., Baker,

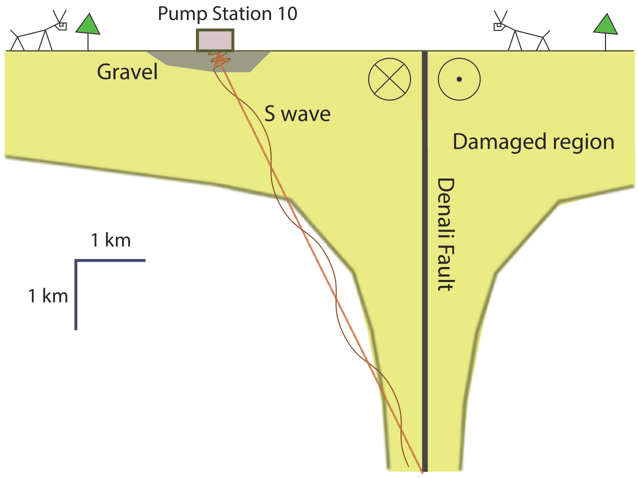

Figure 1. Schematic diagram of the subsurface of PS10 viewed from the west, more or less to scale. *S* waves generated at depth that impinged on PS10 are projected into the plane of the cross section. They accompanied the near-field velocity pulse as both arrived from the west. The waves departed from the deep part of the flower structure of damaged rock at depth and reentered the structure beneath PS10. Brocher et al. (2004) marginally resolved the uppermost part of this structure. A local layer of thin gravel underlies PS10 (thickness exaggerated and locality purely schematic).

2007) as the strong long-period motion and dynamic deformation that accompanies the fault rupture. This usage is distinct from mathematical near-field waves where the amplitude decays with the inverse cube of the distance from a source and intermediate field waves that decay with the inverse square of distance. Ordinary propagating "far-field" body waves decay with the inverse of distance. The response of the rock to near-fault dynamic stresses and strains is highly unlikely to distinguish between these mathematical categories. In addition, this mathematical (purely elastic) partition of waves into near-field, intermediate field, and far-field components no longer strictly applies after the onset of nonlinear behavior.

In general, a recorded earthquake signal originated at depth and eventually traversed the shallow subsurface to the digital seismograph. It is thus necessary to account for source characteristics and shallow linear and nonlinear effects before examining deep nonlinear effects. We discuss the physics of deep nonlinear attenuation in section 2 to put this accountability into context and then return to it in section 7. In particular, conventional nonlinear viscoelastic and plastic rheologies do not preferentially suppresses high-frequency *S* waves, contrary to our observations. We then review the 2002 Denali earthquake where good near-fault records are available for Pump Station 10 (PS10; Ellsworth et al., 2004). PS10 was isolated from other stations, and it is not feasible to infer local source properties independently of its records (Ellsworth et al., 2004). We thus present generally applicable methods that constrain source properties that do not involve nearby stations. Before doing this, we consider ordinary (site-effect) nonlinear attenuation within shallow gravel beneath PS10 to put deeper nonlinear attenuation into context. We examine the records from PS10 to show that strong dynamic strains and stresses associated with the near-field velocity pulse likely brought the uppermost ~2 km beneath PS10 into inelastic failure. We assess unsuccessfully whether coseismic crystalline rock damage occurred beneath PS10 by studying healing of that damage after the mainshock.

We then show that the preferential suppression *S* waves of inferred PS10 at high frequencies are incompatible with simple nonlinear viscoelastic and plastic interaction of the near-field velocity pulse with high-frequency *S* waves within the shallow crystalline rock. We suggest that heterogeneous nonlinear viscoelastic domains interact in parallel within the crystalline rock. In addition, high-frequency *S* waves remained weak at PS10 after the near-field pulse had passed. This observation suggests that high-frequency *S* waves interacted nonlinearly with inelastic deformation associated with the healing of damage as well as directly with the near-field pulse.

This work is intended to aid formulation and interpretation of three-dimensional numerical calculations and the formulation of equivalent material theories for nonlinear behavior of failing and damaged crystalline rock. Our kinematic (where feasible) and dynamic methods are applicable to future better-instrumented earthquakes where more definitive conclusions may be possible.

We mostly apply laterally homogeneous scaling formulations in this paper for brevity and to avoid cloaking simple inferences with onerous mathematics. The structure near PS10 is somewhat laterally heterogeneous (Brocher et al., 2004; Frankel 2004; Kayen et al., 2004). PS10 is near the fault at the side of the flower structure (Figure 1) where the deep geological structure may not be horizontally stratified. We mention lateral heterogeneity when relevant. Generic three-dimensional numerical models related to PS10 seem feasible but very onerous for nonlinear materials, but seismic stations were too widely spaced near PS10 to warrant detailed specific models.

2. Simple Models for Nonlinear Suppression of *S* Waves by the Near-Field Velocity Pulse

We present a simple mathematical model with scaling relationships for the nonlinear suppression of high-frequency *S* waves by the near-field velocity pulse. We make the assumption that the near-field pulse has

Table 1
Shallow Physical Parameters Near Pump Station 10 and Computed Failure Strain

Top depth, m	Bottom depth, m	α, m s^{-1}	β, m s^{-1}	Density, kg m^{-3}	G, GPa	G/z, GPa m^{-1} †	P_{eff}, MPa †	Strain, 10^{-3} †
0 (Gravel)	110	1,800	400	1,800	0.288	0.0052	0.43	1.045
110 (Hard rock)	210	2,500	1,000	2,400	2.4	0.0150	1.55	0.452
210	600	3,750	1,500	2,400	5.4	0.0133	4.91	0.637
600	900	5,100	2,050	2,400	10.09	0.0286	9.64	0.669
900	5,000	5,750	3,330	2,700	29.94	0.0101	45.85	1.072

α is P-wave velocity; β is S-wave velocity; G is shear modulus; † Evaluated at mid-depth z of layer; effective pressure P_{eff} is evaluated from the tabulated densities and the water table at the surface; the failure strains assume a coefficient of friction of 0.7 and the effective pressure. Data from Frankel (2004) partially compiled from the works of Kayen et al. (2004) and Brocher et al. (2004).

much lower frequencies than the *S* waves. That is, we treat the effect of the near-field pulse as imposing a dynamic stress and a dynamic inelastic strain rate that are static on the timescale of the period of the *S* waves. Shaking from the real Denali earthquake was broadband as shown in this paper, so the method is approximate. We consider material (Table 1 and Figure 2) and motion parameters appropriate to PS10 during the 2002 Denali earthquake. This model is adequate for low-frequency nonlinear attenuation of the near-field pulse. In section 7, we discuss more complicated rheology that may also represent observed nonlinear attenuation of high-frequency *S* waves.

We begin by comparing the dynamic stress from the near-field velocity pulse with the dynamic stress from strong high-frequency *S* waves. We apply scaling relationships, which approximately reduce complicated situations to compact equations. These relationships are intended to guide planning and interpretation of three-dimensional numerical calculations. It is helpful to predict the gross magnitudes of effects and to recognize relevant material properties. Here, full numerical calculations of dynamic rupture with frequency ranging from static displacement to ~10 Hz are currently unfeasible in three-dimensions. Computational seismologists thus kinematically add stochastic high frequency sources to low-frequency dynamic models (e.g., Graves & Pitarka, 2016). Trained artificial neutral network methods are also available (Paolucci et al., 2018). It also may be possible to selectively refine nonlinear numerical resolution in the region of interest (Bielak et al., 2003; Yoshimura et al., 2003).

We approximately model the near-field velocity pulse beneath PS10. In general, a task for the seismologist is to infer the distribution and timing of slip on the fault at depth from the surface record. However, dynamic and kinematic models for fault slip near PS10 discussed in section 5.1 do not agree. Neither is the subsurface seismic structure well resolved (Brocher et al., 2004; Frankel 2004; Kayen et al., 2004). Furthermore, station PS10 was too far from other seismic stations to infer its detailed nearby fault slip beneath it independently of its record (Ellsworth et al., 2004).

We thus concentrate on aspects of dynamic strain beneath PS10 that are dimensionally predictable from its record. Clearly, we are making approximations. First, we assume that fault slip is basically horizontal as appropriate for a strike-slip fault. The dominant dynamic displacements are then horizontal. The surface displacement and velocity as PS10 were dominantly horizontal (Ellsworth et al., 2004). The duration of slip at depth on the fault plane, which cuts stiff rock, is long enough that it imposes displacement on the shallow more compliant rock that varies slowly with depth. Figuratively, the shallow compliant rock goes along for the ride. The dominant shallow dynamic strains thus involve horizontal gradients of horizontal displacements. The dominant dynamic stresses produce horizontal shear tractions on vertical planes: τ_{xy} and $(\tau_{xx} - \tau_{yy})/2$, where x and y are horizontal coordinates. The ~100-m gravel layer beneath PS10, however, is thick enough that the near-field velocity pulse may be alternatively treated as an *S* wave refracted into a nearly vertical ray path. The dynamic mean stress $|\sigma| \equiv \sigma_{ii}/3$, where σ is the stress tensor compression positive, then does not change much. We ignore the actual small changes that we do not predict. We caution against applying our scaling relationships that ignore changes in mean stress to dip-slip earthquakes.

2.1. Kinematics of Dynamic Stresses From the Near-Field Velocity Pulse

Roten, Olsen, Cui, and Day, (2017) presented three-dimensional nonlinear numerical models for fault slip and near-fault nonlinear attenuation for generic events similar to the 1992 Landers earthquake. Roten et al. (2014) modeled similar nonlinear near-fault failure for generic San Andreas events, but did not

10.1029/2019JB018386

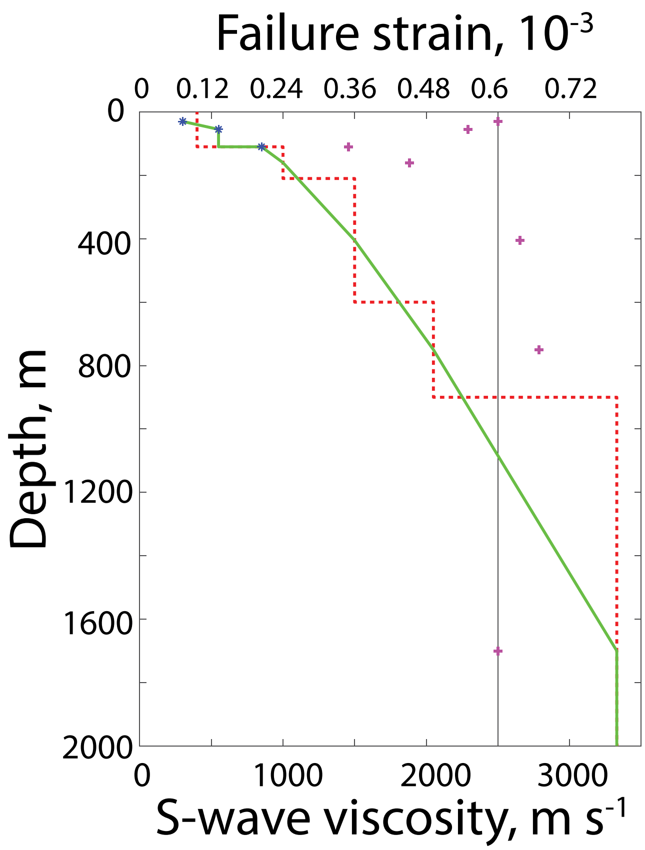

Figure 2. Shear wave velocity as a function of depth. Dashed line is piecewise constant values from Frankel (2004). Solid line approximates the real gradient within the crystalline rock with a step in velocity to the overlying gravel. Crosses are computed failure strains at various depths.

provide cross sections through the fault. These models, where the model fault cuts crystalline rock, are proxies for the Denali fault near PS10. Basically, nonlinear failure occurs within the model flower structure (Figure 1) while the near-field velocity pulse passes. We thus suspect this process beneath PS10. A generic nonlinear numerical model calibrated to PS10 from which dynamic stresses and strains at depth can be extracted would be helpful, but one is not available. As discussed in section 5.1, published linear dynamic and kinematic models for fault slip near PS10 do not agree. Dynamic stresses and strains at depth cannot be readily extracted from these models.

We continue with a well-known dimensional scaling relationship between dynamic stress and dynamic velocity (Sleep, 2016 and references therein). Displacement of the deep stiff rock by the near-field velocity pulse imposes a dynamic strain $\varepsilon_{\text{pulse}}$ on the more compliant rock in the uppermost kilometers. Kinematically, this scalar strain is

$$\varepsilon_{\text{pulse}} \approx \frac{V_{\text{part}}}{c_{\text{pulse}}}, \tag{1}$$

where V_{part} is the scalar particle velocity and c_{pulse} is the phase velocity of the pulse, which is essentially the rupture propagation velocity. The relationship is everywhere exact for a kinematic wave with y (fault perpendicular) displacement that propagates in the x-direction, which is fault parallel, $D_{\text{dyn}} = D_y(x - c_{\text{pulse}}t)$ and is time and approximately valid otherwise. (Comparable, fault-normal and fault-parallel velocity components were observed at PS10 (Ellsworth et al., 2004). The dynamic stress is the strain times the shear modulus

$$\tau_{\text{pulse}} = G\varepsilon_{\text{pulse}} \approx \frac{GV_{\text{part}}}{c_{\text{pulse}}}, \tag{2}$$

where the shear modulus G may be a function of depth.

Equations (1) and (2) are approximately correct, as they are closely related to Rayleigh's principle (e.g., Jeffreys, 1961) that the overall elastic energy per volume $\tau^2/2G$ (here for an S wave where τ is dynamic stress) equals the overall kinetic energy per volume $\rho V^2/2$, where ρ is density and V is dynamic velocity. For a plane wave in a homogeneous medium, the dynamic stress is locally and exactly $\tau = \rho V \beta$, where $\beta = \sqrt{G/\rho}$ is the group (and phase) velocity of the S wave. This relationship (which is a special case of (2)) applies approximately in more complicated situations, for example, near to the rupture tip on the fault during an earthquake. The peak dynamic stress and the peak dynamic velocity then do not occur at exactly the same place and time (Andrews, 2004, 2005; Cocco et al., 2009; Tinti et al., 2004).

In our case, we have detailed information on the seismic waves only at the surface station PS10; other seismic stations were too far away to provide insight (Ellsworth et al., 2004). The predictable aspect of the phase velocity is that the near-field pulse propagates horizontally parallel to the fault trace at the rupture velocity, which grossly scales with the S-wave velocity of deep (>2 km) crystalline rocks along the fault plane and is here crudely 3.5 km s^{-1}. As discussed in Section 5.2, linear models of the rupture do not agree and a more precise nonlinear constraint is not available. The measured peak ground velocity (PGV) of ~1.8 m s^{-1} (Ellsworth et al., 2004) provides a proxy for the peak particle velocity at depth. We show that this proxy likely underestimates the particle velocity of the pulse within the crystalline basement in Sections 5.1 and 5.5. That is, the (~2 km) deep dynamic deviatoric strain from (1) is crudely 1.8 m s^{-1}/3.5 km s^{-1} = 0.5×10^{-3}, which we use in subsequent example calculations.

2.2. High-Frequency Dynamic Stresses With the Crystalline Rock

We begin the discussion by showing that the dynamic stresses within the crystalline rock from high-frequency S waves are typically less than the low-frequency dynamic stresses from the near-field velocity

10.1029/2019JB018386

pulse. Furthermore, it is likely that the uppermost ~2 km of crystalline rock is pervasively cracked, as its *S*-wave velocity is less than that of the underlying intact rock (Figure 2). We discuss the effective rheology of this crystalline rock in sections 2.3 and 7. We return to the origin of these cracks in section 5.

We provide a simple example calculation to show that dynamic shear strains and shear stresses from the near-field velocity pulse are much greater than those from high-frequency *S* waves. For the near-field pulse, we assume dynamic strain of 0.5×10^{-3} from sections 2.1 and 5.1 for PS10 and shear modulus of 30 GPa for crystalline rock from Table 1 to obtain 15 MPa, as an example. There are likely no strong reflective interfaces within the crystalline rock (Figure 2). Plane waves provide a simple approximation for high-frequency body waves. The dynamic stress for (here high-frequency) *S* waves is $\tau_{\mathrm{dyn}} = \rho\beta V_{\mathrm{dyn}}$, where V_{dyn} is the dynamic (particle) velocity to distinguish it from V_{part}, ρ is density, and β is *S*-wave velocity. We assume very strong *S* waves as an example, as our goal is to show that the dynamic stress from these waves is small compared to that from the near-field velocity pulse, rather than to provide a precise estimate of their actual dynamic stresses. Our model *S* waves have a dominant frequency of 10 Hz with a peak dynamic acceleration A_{dyn} of 1 g within the crystalline rock. The peak model dynamic velocity is $V_{\mathrm{dyn}} \approx A_{\mathrm{dyn}}/\omega = 0.156$ m s^{-1}, where ω (here 62.8 s^{-1}) is the dominant angular frequency. We let the deep density be 2700 kg m^{-3} and the *S*-wave velocity be 3330 m s^{-1} from Table 1. The peak dynamic stress is 1.39 MPa, which is far less than that from the near-field pulse.

Note that the dynamic acceleration of our model *S* wave would be far greater than 1 g when it arrived at the free surface through an elastic medium. First, the free surface doubles the acceleration relative to that of the impinging wave at depth. Second, energy is approximately conserved within a wave passing through a gradual gradient (see Goto et al., 2011), here in the crystalline rock (Figure 2). The vertical energy flux scales as $0.5\rho\beta V_{\mathrm{dyn}}^2$. The dynamic velocity and hence dynamic acceleration at the dominant frequency scales with inversely the square root of the seismic impedance $\beta\rho$ and hence accelerations are higher within the shallow low-velocity rock. A precise estimate of this amplification needs to be reduced as the ascending waves partly reflected from the top of the crystalline rock. The actual reflection coefficient is not precisely constrained.

The observed high-frequency *S* waves recorded at PS10 were far weaker than 1 g (Ellsworth et al., 2004). However, *S* waves of nearly this strength arrived at Lucerne during the 1992 Landers earthquake (Chen, 1995; Iwan & Chen, 1995), which gives plausibility that the Denali source did generate strong *S* waves that subsequently attenuated before reaching PS10. We proceed assuming that the dynamic stress from high-frequency *S* waves beneath PS10 was much less than the dynamic stress from the near-field velocity pulse.

2.3. Effective Inelastic Rheology for the Near-Field Velocity Pulse and the High-Frequency *S* Waves

The weak dynamic stresses from the high-frequency *S* waves propagated through the strong low-frequency dynamic stresses from the near-field velocity pulse. We thus begin with the inelastic effects of the stronger stresses and then consider the weaker stresses as perturbations. For now, the macroscopic inelastic behavior of the crystalline rock is the cumulative effect of inelastic failure of numerous variously oriented cracks.

Off-fault aftershocks triggered by static stress changes (Cattania et al., 2015) provide analogy to crack failure from the near-field pulse. Aftershocks preferentially occur on small faults with preexisting stresses that are favorably oriented with respect to Coulomb failure driven by the static change in the stress tensor. The tendency for failure depends very nonlinearly on the resolved stress on the small faults. The enhancement of seismicity on favorably oriented faults greatly exceeds the diminution of seismicity on unfavorably oriented faults. Specifically, earthquakes on faults that are favorably oriented relative to normal traction changes preferentially occur, which reduces the effect of mean stress on overall macroscopic seismicity. In addition, the static stress changes that trigger off-fault aftershocks are typically far less than those needed to cause earthquakes within unstressed rock. Physically, earthquakes are complicated. Stress drops (as opposed to ideal plastic behavior) have likely occurred previously within the aftershock-hosting region, causing both weakly stressed faults (that remain quiet) and prestress concentrations on other faults (that host aftershocks). The sense of aftershock slip is preferentially that to relieve both the local prestress and the broad static stress change.

Lessons regarding inelastic failure qualitatively involve replacing small faults with cracks and static stress change with low-frequency dynamic stress in the previous paragraph. Cracks with orientations favorably oriented with respect to the low-frequency dynamic stress preferentially fail. Slip on the cracks preferentially has the sense to relax the instantaneous dynamic shear traction on the cracks and to nonlinearly attenuate the seismic wave. Such inelasticity failure may be viewed as virtual double-couple sources of new seismic waves (Ben Zion & Lyakhovsky, 2019).

In addition, macroscopic failure commences at somewhat low dynamic stresses before the Coulomb failure criterion is reached for unstressed cracks. That is, favorably prestressed cracks fail at weak dynamic stresses in analogy to off-fault aftershock. The strengths (coefficients of friction) of numerous pervasive cracks in the crystalline rock also likely vary; clearly cracks should be weaker than intact rock. The net macroscopic effect of these processes is that the inelastic strain rate within the cracked rock increases somewhat gradually with dynamic stress, rather than exhibiting a sharp plastic failure criterion (Sleep, 2010).

We continue by considering the perturbation of the inelastic strain rate owing to the strong dynamic stresses of the near-field velocity pulse by the weak high-frequency *S* waves. That is, we consider the cumulative effects over numerous cracks that are already failing from the stronger dynamic stress. A lesson from aftershocks carries through: failure preferentially occurs when the high-frequency dynamic stress is favorably oriented relative to the low-frequency stress driving failure. The net effect is that enhanced slip preferentially relaxes the instantaneous high-frequency dynamic stress, nonlinearly attenuating the high-frequency waves. Conversely, high-frequency dynamic stress that is antithetic to the low-frequency dynamic stress slows the total slip rate; the net high-frequency perturbation is antithetic slip that with the sense to relax the instantaneous antithetic stress. A high-resolution numerical model that included the elastic and inelastic rheology of individual cracks and prestresses within pervasively cracked rock cannot be readily be computed. We thus semiquantitatively continue with the effective inelastic rheology of the rock mass. The rounded values of *S* wave velocity of 2000 m s^{-1} and 10 Hz frequency imply a 50 m quarter-wavelength scale for an equivalent medium.

For a simple demonstration, we apply a Drucker and Prager (1952) rheology based on the second invariant $|\tau| = \sqrt{\tau_{ij}\tau_{ij}}$ of the deviatoric stress tensor τ for an isotropic material. The assumption of isotropy seems reasonable for grain-grain contacts in gravel and maybe for pervasively cracked crystalline rock in the uppermost basement, and we lack information on inelastic anisotropy beneath PS10. The *S*-wave Roten et al. (2014, 2016; Roten, Olsen, Cui, & Day, 2017; Roten, Olsen, & Day, 2017; Wang et al., 2019) used this rheology in three-dimensional numerical models.

For brevity of discussion, we assume that only the deviatoric stress changes and thus ignore strong *P* waves, which is crudely appropriate at low frequencies for a strike-slip earthquake. The inelastic strain rate tensor is then aligned with the deviatoric stress,

$$\varepsilon'_{ij} = \varepsilon'_0 \left[\frac{\tau_{ij}}{|\tau|}\right] F(|\tau|) = \frac{\tau_{ij}}{2\eta_{\mathrm{app}}}, \tag{3}$$

where the material parameter ε'_0 has dimensions of strain rate and the bracket aligns strain rate and deviatoric stress tensors. F is a strong dimensionless function of the second invariant that in general also depends on the effective mean stress $|\sigma| \equiv \sigma_{ii}/3 - P_{\mathrm{fluid}}$, where σ is the stress tensor (compression positive) and P_{fluid} is the fluid pressure, in a Coulomb material. The right-hand equality introduces the apparent viscosity for nonlinear rheology $\eta_{\mathrm{app}} \equiv |\tau|/2F(|\tau|)\varepsilon'_0$ for a nonlinear material.

We proceed without complicating this simple well-known rheology. Nonlinear flow laws are widely used in geodynamics, including mantle deformation (e.g., Turcotte & Schubert, 2002, Chapter 7), but not in geotechnical engineering, which has been developed for shallow soils and not for deep crystalline rock.

We compare an ideal plastic rheology, which has no rate dependence. Geotechnical applications often apply Masing-type rheology. The initial low-amplitude strain in one horizontal dimension is proportional to the stress, $\tau = G_{\mathrm{int}}\varepsilon$, where G_{int} is the elastic shear modulus. Predicted stress-strain trajectories are not rate dependent, one gets the same trajectory at 1000 and 0.001 Hz. However, frequency-dependent and hence rate-dependent behavior are observed in the laboratory for both clay (Afacan et al., 2014) and sand (Güler & Afacan, 2019). Menq (2003) studied Masing-type behavior of gravel but did not measure frequency-dependent effects. We are not aware of relevant data on crystalline rocks.

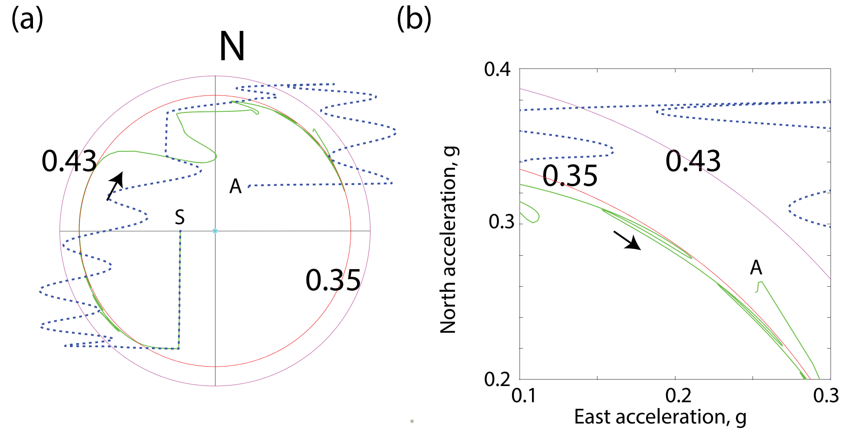

Figure 3. Polar diagrams of computed surface normalized acceleration from Appendix A. Resolved normalized accelerations of 0.43 and 0.35 are shown as circles for reference. The circularly polarized signal begins at S and ends at A. The linear model (dashed line) shows strong amplitudes between SW and W, when only the direct wave arrives. The amplitude is weak between W and N when the reflection from the base of the surface layer destructively interferes with the direct signal. The reflected arrival constructively interferes with the direct wave between N and WNW. The curve for the nonlinear model (solid line) clips near 0.35 g and is not simply related to the linear curve. (a) Full polar diagram. (b) NE region of Figure 3a windowed so that high-frequency loops in the nonlinear signal are evident.

Equation (3) reduces to an ideal plastic rheology when F is an extremely strong function of $|\tau|$. That is, inelastic strain rate ε' is effectively zero for the problem of interest for stresses less than the failure stress $|\tau| < \tau_{\mathrm{fail}}$, so the material is linearly elastic. The strain rate is unobtainably large for $|\tau| > \tau_{\mathrm{fail}}$. Therefore, the stress $|\tau|$ may equal but not exceed the failure stress.

We follow Roten et al. (2014), who formulated their nonlinear models with (3) in this way to approximately represent ideal plasticity with a more numerically convenient flow law. We numerically model vertical ascending S waves to illustrate basic features of plastic rheologies when strong low-frequency waves and weak high-frequency waves impinge together on the free surface (Appendix A). The normal traction on horizontal planes of failure does not change in this case. As noted in the previous paragraph, equation (3) in the limit that F is a very strong function of stress reduces to a plastic failure envelope. The plastic potential then reduces to $f = 3\left(\tau_{xz}^2 + \tau_{yz}^2\right)$, where x and y are horizontal coordinates and z is depth (e.g., Hill & Orowan, 1948, equation (3)). In general, the plastic potential in the absence of mean stress changes is a constant times $\sqrt{\tau_{ij}\tau_{ij}}$, so (3) correctly represents the orientation of the inelastic strain rate tensor. Obviously, mean stress changes can be included in full three-dimensional numerical models (e.g., Roten et al., 2014).

Our numerical model in Figure 3 illustrates the behavior of a strong high-frequency component and a weak high-frequency component in a nearly plastic material. Our model region crudely represents the uppermost subsurface beneath PS10 as half-space with 800 m s^{-1} S-wave velocity under a lid with an S-wave velocity of 400 m s^{-1} to the (110.25 m deep) base of the gravel in Figure 2. We impose vertically ascending S waves that are circularly polarized in the half-space with a peak acceleration of 0.114 g and a period of 1.5 s. The long-period acceleration of the near-field velocity pulse at PS10 was circularly polarized (Figure 2). Weak waves with 0.2 of that peak acceleration and a period of 0.1 s impinge through the half-space with east-west motion. Our arbitrary high-frequency east-west polarization in Figure 3 imposes components parallel to and normal to the long-period acceleration at times when it is strong. The effective coefficient of friction is ~0.35 in the model.

The model illustrates the basic feature that the resolved horizontal acceleration clips at the imposed effective coefficient of friction of ~0.35 (Figure 3a). In addition, the model illustrates the general behavior of high-frequency signal with plastic rheology. During certain times of the shaking, the near-field velocity pulse has locally brought the Coulomb medium up to the failure criterion. One high-frequency component of S wave causes a horizontal shear traction that is normal to that of the near-field velocity pulse. This transient stress component does not change the total shear traction $|\tau|$ away from the failure criterion. It does rotate

10.1029/2019JB018386

the direction of the resolved shear traction, producing loops in the acceleration curve (Figure 3b). We assume (in Appendix A) very strong rate dependence on stress in F (rather than ideal plasticity) so that these loops are visible in Figure 3b.

In more detail, S waves effectively reflect from the depths where nonlinear attenuation is happening. Equivalently, the inelasticity strain from nonlinear attenuation may be viewed as virtual double-couple sources of new seismic waves (Ben Zion & Lyakhovsky, 2019). The reflected (or secondary) waves then reflect from the free surface and reflect from the top of the half-space. Failure occurs at various depths and not always at the same time. The nonlinear signal is thus related to the impinging signal in complicated way. A general conclusion from the model is that some high-frequency energy reaches the surface when the medium is ideally plastic. Three-dimensional behavior is similar but more complicated.

In the example, the component of high-frequency shear traction τ_{orth} on horizontal planes that is orthogonal to low-frequency shear traction from the near-field pulse negligibly adds to the invariant as $|\tau| = \sqrt{\tau_{\text{pulse}}^2 + \tau_{\text{orth}}^2}$ and is not suppressed. Here, the high-frequency S waves are suppressed somewhat with a plastic rheology, but some high frequency still propagates. There is also some apparent anisotropy depending on the stress tensor from the near-field pulse in the suppression in analogy to the directional anisotropy in Figure 3 where the component parallel to the circle propagates. The effect of changes in the mean stress needs to be included in the inelastic strain tensor in (3), if strong P waves are present. Overall, there is no simple increase of nonlinear attenuation with frequency.

The case when F is a mildly nonlinear function of $|\tau|$ is similar but complicated in three dimensions. The strong deviatoric stress tensor from the near-field velocity pulse τ_{pulse} varies slowly with time, and a weaker deviatoric stress tensor $\Delta\tau_S$ from the S wave oscillates rapidly. We distinguish the apparent viscosity in (3) from the differential viscosity η_{diff} which is related to the change in the strain rate from $\Delta\tau_S$ strain. The problem reduces to scalars when τ_{pulse} and $\Delta\tau_S$ align. The change in strain rate is then

$$\Delta\varepsilon' = \varepsilon_0' \frac{\partial F(\tau)}{\partial \tau} \Delta\tau_S \equiv \frac{\Delta\tau_S}{\eta_{\text{diff}}}. \tag{4}$$

For a strongly nonlinear rheology, $\partial F/\partial\tau > > F(\tau)/\tau$ and the differential viscosity are much less than the apparent viscosity. The three-dimensional analog of (4) involves differentiation of (3) for each component of the stress tensor. The result is complicated and not particularly revealing. We qualitatively point out some attributes: (1) All terms of the stress tensor occur in $|\tau|$; The cross terms with $kl \neq ij$ of $\left(\partial\varepsilon'_{kl}/\partial\tau_{ij}\right)$ are nonzero. (2) The perturbation $\Delta\tau_{S,\text{orth}}$ might be orthogonal to $\tau_{\text{pulse},}$. Then the invariant within F in (3) does not change for small high-frequency perturbations. The perturbation to strain rate aligns with perturbing high-frequency stress:

$$\Delta\varepsilon'_{\text{orth},ij} = \varepsilon'_{S,ij} \approx \varepsilon'_0 \left[\frac{\Delta\tau_{S,ij,\text{orth}}}{|\tau_{\text{pulse}}|}\right] F\left(|\tau_{\text{pulse}}|\right). \tag{5}$$

The differential viscosity for this perturbation is then the differential viscosity in (3) $|\tau_{\text{pulse}}|/2\varepsilon'_0\left[F\left(|\tau_{\text{pulse}}|\right)\right]$.

That is, the instantaneous rheology for the small high-frequency perturbations $\Delta\tau_S$ is linearly viscous but aniosotropic. Returning to scalars, a linear viscous material with linear elasticity (a Maxwell body) does not preferentially attenuate high-frequency waves. We return to this topic in section 7 after we have discussed observations of the apparent attenuation of high-frequency S waves beneath PS10.

For comparison, Harper-Dorn creep is an analogous form of pseudolinear behavior in a nonlinear material, where the strong stress oscillates and the weaker stress is more static (Weertman & Blacic, 1984). For the near-field pulse, the strong stress is more static, and the weak stress from S waves oscillates. In both cases, the stronger stress determines the invariant in (3), and the material responds apparently linearly to the weaker stress.

10.1029/2019JB018386

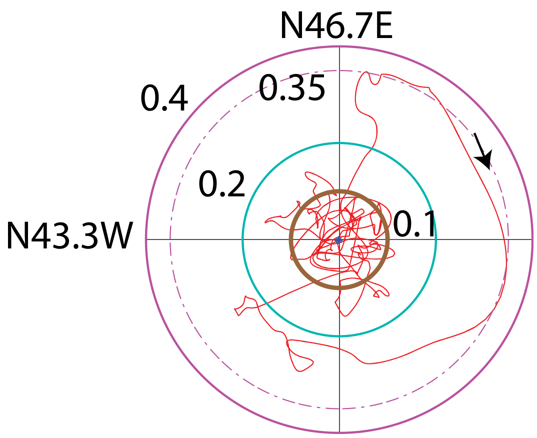

Figure 4. Polar plot of dynamic acceleration recorded between 14 and 22 s after the initial *P* wave to window signal associated with the near-field velocity pulse. The strongest signal is circularly polarized in a clockwise sense for 1/3 of a cycle between 0300 and 0430 hr. Circles indicate normalized accelerations centered on the origin. The high-frequency component parallel to the semicircular acceleration path does not change the resolved acceleration much and is not suppressed (Sleep & Nakata, 2015). Weak loops and kinks in the acceleration curve subparallel to the main trend at 0100, 0700, and 0800 hr may be associated with an unsuppressed weak high-frequency component.

3. PS10 Records

We examine real data with forethought to appraise our inferences on nonlinear attenuation in section 2. Digital seismographs at PS10: Latitude = 63.4244944°N, longitude = −145.762664°E, and elevation = 726.1 m (Ellsworth et al., 2004; Evans et al., 2006) recorded the 03 November 2002 M_w = 7.9 Denali earthquake. Martirosyan et al. (2004) give 63.4239°N,−145.7658°E, which is self-consistent with the datum used by Carver et al. (2003) to locate temporary stations. This station was ~3 km north of the surface rupture (Figure 1) with strike-slip displacement of ~5 m (Eberhart-Phillips et al., 2003; Hreinsdottir et al., 2003; Dreger et al., 2004; Frankel 2004; Haeussler et al., 2004; Kayen et al., 2004; Oglesby et al., 2004; Wright et al., 2004; Asano et al., 2005; Liao and Huang, 2008; Walker & Shearer, 2009). Rupture approached PS10 from the west-northwest.

Ellsworth et al. (2004) corrected the PS10 records for instrument response, electronically digitized at 200 points per second. Their record lasts until 83.67 s after the onset of the *P* wave. The instrument then apparently ceased operation and did not record any subsequent aftershocks. They and Martirosyan et al. (2004) noted that the high-frequency acceleration (Peak Ground Acceleration, PGA) of 0.35 g was weak for a station within 3 km of a major fault with 1.8 m s^{-1} dynamic velocity (Peak Ground Velocity, PGV) and ~5 m of slip. In more detail, PGA is associated with long-period motion from the near-field velocity pulse not from high-frequency *S* waves (Figures 4 and 5). The high-frequency *P* waves before the near-field pulse are stronger than the *S* waves (Figure 5).

Ellsworth et al. (2004) qualitatively attributed the weak PGA and the general weakness of high-frequency *S* waves to nonlinear attenuation within the surface gravel layer (Table 1). We quantify this inference in section 4. Our main purpose is to examine apparently nonlinear suppression of high-frequency *S* waves by the near-field velocity pulse, mainly within the underlying crystalline rock in section 5 (Sleep & Nakata, 2015). The shallow-nonlinearity mechanism is well known from sites with better records (Ghofrani et al., 2013, Wu & Peng, 2011; Nakata & Snieder, 2011; Assimaki et al., 2008; Sleep & Nakata, 2017; Bonilla et al., 2019). We discuss it to put the nonlinearity associated with the near-field velocity pulse, which is not well documented elsewhere, into context. This paper is intended in part to illustrate generally applicable methods for more constrained future near-fault records.

4. Shallow *S*-Wave Nonlinearity Within the Gravel

We use traditional methods to examine shallow nonlinearity beneath PS10. The seismic velocities and densities (Table 1 and Figure 2) were obtained in a piecewise constant manner by Frankel (2004) from the works of Kayen et al. (2004) and Brocher et al. (2004). The approximately 110 m thick unlithified gravel beneath the station is a real layer. There is likely a sharp step from the low velocities in the gravel to higher velocities in crystalline rock, which reflected body waves. The other tabulated layers of crystalline rock are likely approximations for a gradient. The solid smooth line in Figure 2 is likely a better representation of the subsurface than the piecewise constant dashed line by Frankel (2004).

The low seismic velocity of the gravel simplifies the analysis of short-period signal. Shallow rays refracted into nearly vertical paths under PS10. We begin with scaling relationships for exactly vertical body waves. We start with the approximation that the high-frequency horizontal signal is mainly *S* waves, and the high-frequency vertical signal is mainly *P* waves. We have no better way to separate coarriving *S* waves from *P* waves. Methods that depend on the ratio of the vertical to the horizontal amplitude of *S* waves are applicable because we cannot remove *P* waves from the vertical signal (e.g., Carpenter et al., 2018). Methods that require borehole stations are inapplicable. We first examine data from PS10 in the time domain. We then look for before- and after-shaking changes in the shear modulus of the gravel in the frequency domain.

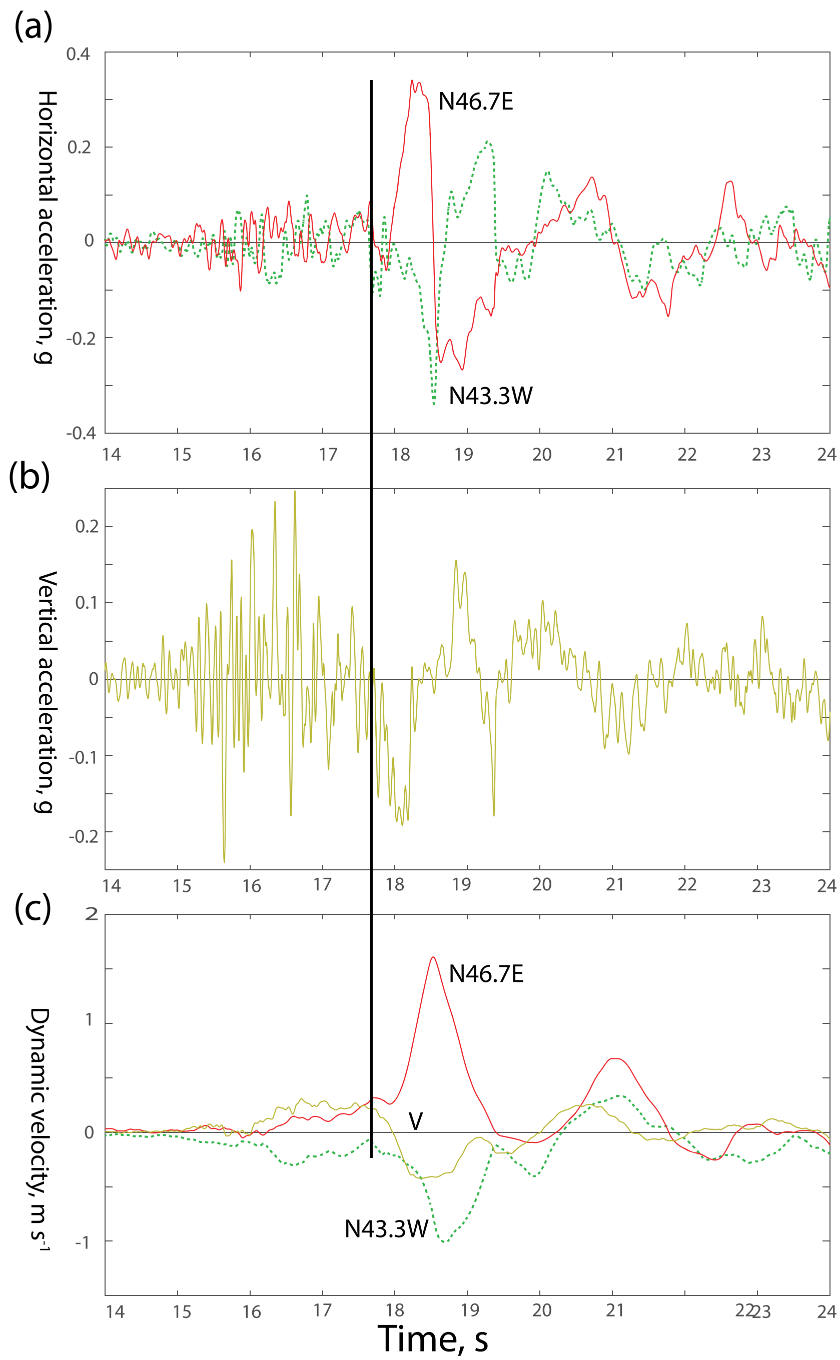

Figure 5. Digital seismograms for PS10; times are relative to the initial *P* wave from Ellsworth et al. (2004). Vertical line marks the approximate start of the near-field velocity pulse. (a) Horizontal dynamic acceleration for the N43.3 W and N46.7E recorded components. (b) Vertical dynamic acceleration. (c) Dynamic velocities.

4.1. Application of Scaling Relationships in the Time Domain

Simple scaling relationships for nonlinear behavior of body waves apply in the time domain. Vertically propagating *S* waves produce shear tractions on horizontal planes. If these tractions are sufficiently high, nonlinear shear failure occurs on these planes. We examine the nonlinearly dissipation of energy along these planes with regard to nonlinear attenuation of the Denali *S* waves in this subsection. We examine transient seismic velocity changes from damage associated with inelastic strain in the gravel in subsection 4.2. We use simple friction without cohesion, which may be appropriate for shallow gravel with grain-to-grain constants. We also assume a laterally homogeneous isotropic medium for now and return to the issue of lateral heterogeneity in subsection 4.2.

A well-known scaling relationship states that the normalized acceleration (that in g's) is approximately equal to the Coulomb ratio between dynamic shear traction and effective lithostatic stress. To see the basis of this relationship following Sleep and Nakata (2017), the (one-dimensional) momentum equation indicates that the resolved horizontal acceleration is everywhere proportional to the vertical gradient of the horizontal shear traction:

$$\rho A_h = \frac{\partial \tau_{hz}}{\partial z}, \tag{6}$$

where h is the tensor index for the resolved horizontal direction, ρ is rock density, A is acceleration, τ is the stress tensor, and z is depth. At frictional failure, the failure stress is

$$\tau_{\text{fail}} = P_{\text{eff}}\mu \approx \mu(\rho - \rho_w)gz, \tag{7}$$

where τ_{fail} is the failure stress from friction, μ is the coefficient of friction, the effective pressure P_{eff} is the difference between lithostatic pressure and fluid pressure, and g is the acceleration of gravity (~9.8 m s^{-2}). The approximate equality assumes that rock density ρ and water density ρ_w are constant with depth z. The model water table is at the surface as approximately beneath PS10 (Kayen et al., 2004; Martirosyan et al., 2004). The strong wave brings the shallow subsurface into failure. The vertical gradient of failure stress then equals the vertical gradient of the resolved shear traction:

$$\frac{\partial \tau_{\text{fail}}}{\partial z} \approx \mu(\rho - \rho_w)g = \frac{\partial \tau_{hz}}{\partial z} = \rho A_h. \tag{8}$$

Solving yields

$$\left|\frac{A_h}{g}\right| \leq \left[\frac{(\rho - \rho_w)}{\rho}\right]\mu \equiv \mu_{\text{eff}}, \tag{9}$$

that is, the normalized acceleration equals the effective coefficient of friction μ_{eff}. A testable prediction is that the normalized acceleration of a train of strong S waves will clip repeatedly at the effective coefficient of friction, as shown by the model in Figure 3.

In terms of (3), macroscopic failure may involve numerous grain-grain contacts within the gravel and numerous minor cracks with the crystalline rock. The failure strengths and inelastic creep rates on these contacts and cracks may vary over a range. Some contacts and cracks begin to fail at lower dynamic stresses than others. A testable prediction is then that the macroscopic inelastic strain rate increases somewhat gradually with dynamic stress. There then will be a tendency for the S waves to peak at normalized accelerations around μ_{eff}, rather than to sharply clip at an ideal coefficient of friction.

A similar relationship applies to P waves. The ratio between dynamic normal traction and lithostatic stress is the normalized vertical acceleration. Downward accelerations of above 1 g bring the rock into horizontal tension greatly reducing its strength for S waves (Aoi et al., 2008; Yamada et al., 2009; Tobita et al., 2010; Kinoshita, 2011; Bradley & Cubrinovski, 2011; Goto et al., 2019). Such P waves tend to clip at dynamic downward accelerations above 1 g in the Earth and in numerical models. We ignore this effect for brevity, as the P waves were relatively feeble during the near-field velocity pulse at PS10 (Ellsworth et al., 2004; Figure 5).

Figure 4 shows the predicted behavior in (9) for the near-field velocity pulse at PS10 as modeled in Figure 3. The dynamic acceleration is circularly polarized near PGA of ~0.35 g for one third of a cycle lasting ~0.35 s. For reference, the resolved acceleration remained above 0.2 g for ~1.25 s. The source model of Ellsworth et al. (2004) does not imply clipping at 0.35 g. The component perpendicular to the loop that augments resolved acceleration is suppressed. Conversely, the component of acceleration parallel to the loop does not greatly

10.1029/2019JB018386

add to the resolved acceleration and thus is not suppressed (Figure 3b). A strong component that reduces resolved acceleration is also not suppressed. One would expect strong loops in Figure 4, like in Figure 3, if strong high-frequency *S* waves were present. These features also occur in numerical models of shallow nonlinear *S* waves (Sleep & Nakata, 2017). However, only weak kinks and loops occur subparallel to and perpendicular to the track (Figure 4).

The model in Figure 3 involves formulism for high-frequency *S* waves, while the observed frequency range includes the near-field velocity pulse. Thus, clean partition of signal into these categories is not productive. We discuss the kinematic effect that nonlinear attenuation of the near-field velocity pulse causes the long-period particle velocity at surface to be less than that at the base of the gravel in section 5.1.

The observed clipping at ~0.35 g (Figure 4) implies a reasonable effective coefficient of friction μ_{eff} of ~0.35. The water table was near the surface at PS10 in 2002 (Kayen et al., 2004; Martirosyan et al., 2004). For $\rho =$ 1800 kg m^{-3} (Table 1), $\rho_w = 1000$ kg m^{-3}, and a generic coefficient of friction of 0.7, the predicted effective coefficient of friction is 0.31. Given that these parameters are somewhat uncertain, there is an agreement between observation and prediction. For example, increasing the gravel density to 2000 kg m^{-3} or its coefficient of friction to 0.79 yields an effective coefficient of friction of 0.35.

4.2. Search in the Frequency Domain for Damage Within Gravel

Body waves should resonate within the shallow low-velocity gravel layer, provided that there is a strong seismic velocity contrast with the underlying crystalline rock. The resonant frequency within the layer decreases when damage from strong shaking decreases the shear modulus *G* and hence the *S*-wave velocity β (Ghofrani et al., 2013, Wu & Peng, 2011; Nakata & Snieder, 2011; Assimaki et al., 2011; Sleep & Nakata, 2017; Bonilla et al., 2019). The resonant frequency for *P* waves may also decrease (Han et al., 2015). In both cases, the resonant frequency typically increases as the damaged gravel heals in the aftermath of the strong shaking.

The predicted resonant frequency for *S* waves is $\beta_g/4Z_g$ where β_g is the *S*-wave velocity of the gravel and Z_g is the thickness of the gravel layer. The analogous resonant frequency for *P* waves is $\alpha_g/4Z_g$, where α_g is the *P*-wave velocity of the gravel. For the parameters in Table 1, these frequencies are 0.91 and 4.1 Hz, respectively. There is no colocated borehole station at PS10, so surface to borehole spectral ratios cannot be used to study resonance; we have no other good way to infer the detailed effects of the source on the spectra of the PS10 impinging waves. Our predictions still tell approximately where to look for resonances on the digital spectrograms. They provide hints on how to associate spectral peaks with ray paths. All spectra in this section were obtained from signal over 10.24 s durations tapered at both ends by a 0.64 s cosine.

Spectra for the interval 0 to 10.24 s after the initial *P* wave show the low-amplitude response before strong shaking (Figure 6a) for later comparison with the time of the near-field velocity pulse from 16 to 26.24 (Figure 6b) and its high frequencies (Figure 6c). One would expect that *P* waves would dominate the 0 to 10.24 s record. There still should be *S* waves converted from *P* waves that arrived before the direct *S* waves. *P* waves should dominate the vertical component in laterally homogeneous structure, and *S* waves should dominate the horizontal components.

Foreshock and aftershock digital data would help constrain the prequake low-amplitude shallow velocity structure beneath PS10 and healing of any damage after the mainshock. Carver et al. (2003) recorded aftershocks at temporary stations near PS10. We discuss these data in section 6. We have no foreshock data.

The low-amplitude signal of the mainshock data shows expected effects for resonating waves within the gravel. The N43.3 W component shows a strong peak centered at 1.2 Hz. The vertical component has a strong peak at 4.8 Hz. Retaining the seismic wave velocities from Table 1 yields estimated gravel thicknesses of 83 and 94 m, respectively. Retaining the thicknesses yields seismic velocities of 528 and 2112 m s^{-1}, respectively. That is, the inferred thickness and seismic velocities of the gravel layer underneath PS10 are near to but not precisely those in Table 1. There is a gross agreement given that the tabulated velocities are in the region of PS10 and not precisely underneath that station. Dunham and Archuleta (2004) noted that the shallow low-velocity layer is laterally heterogeneous near PS10, as strong surface waves did not build up within the layer.

However, the 1.2 Hz peak on the N43.3 W component does not appear on the N46.7E component. In addition, the N46.7E component shares the 4.8 Hz peaks with the vertical component. There is also a weak peak at 4.8 Hz on the N43.3 W component. The horizontal components of PS10 were within 0.2° of horizontal, too

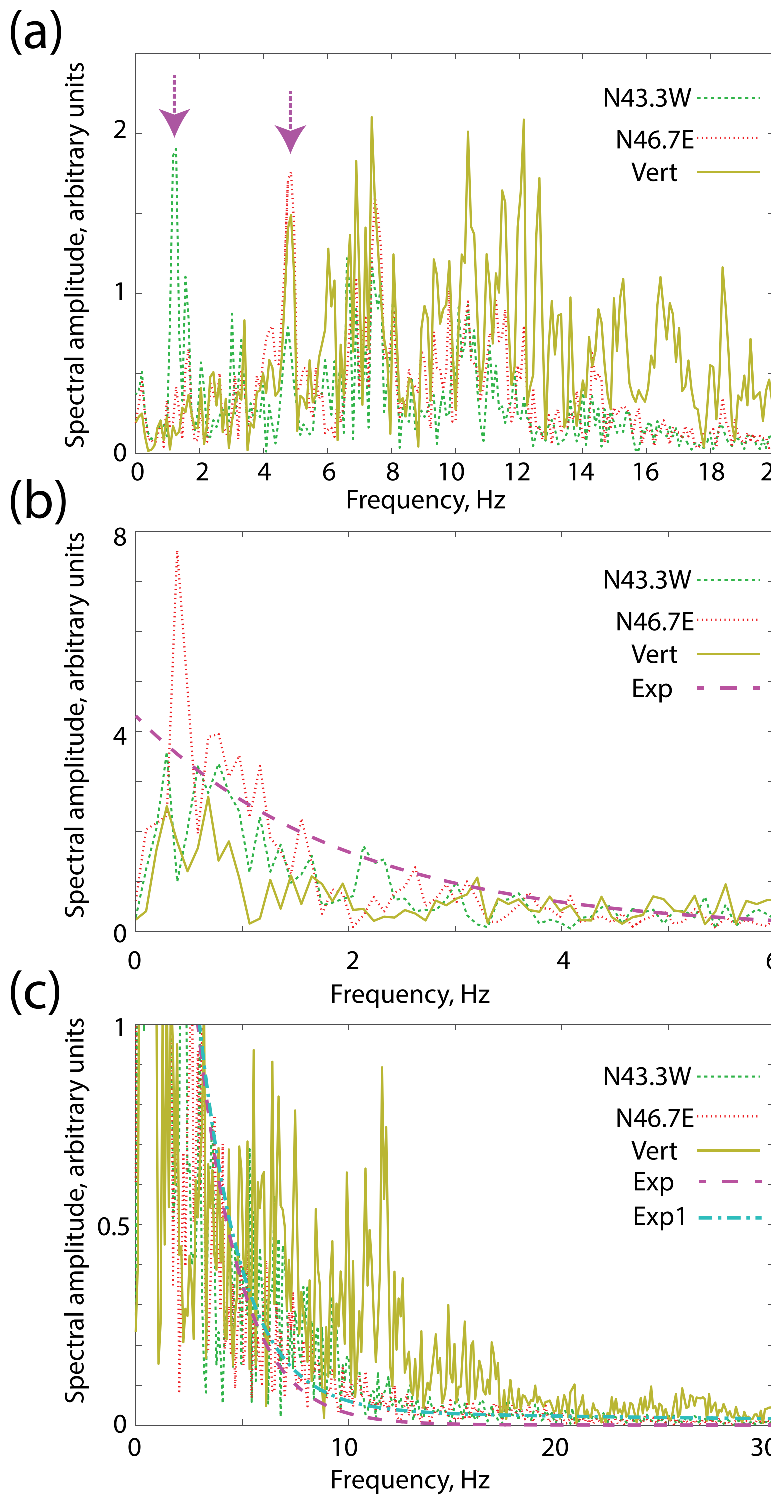

Figure 6. Spectral acceleration amplitudes for PS10 are arbitrary but consistent between traces and panels. (a) The 0 to 10.24 s (after *P*) interval: A spectral peak near the expected *S*-wave reverberation frequency is at ~1.2 Hz on the N43.3 W record. The expected *P*-wave reverberation is present near 4.8 Hz. This peak is also present on the horizontal N46.7E component, indicating that the structure is not laterally homogeneous. (b) The 16–26.24 s interval of the near-field pulse: Most of the signal has frequencies lower than the predicted 1.2 Hz resonance. No resonances are evident. An exponential curve proportional to $\exp(-t_0 f)$, where f is frequency and $t_0 = 0.5$ s is shown for comparison with the horizontal spectra. (c) High frequencies in 16-26.24 s interval windowed from panel b: Exponential curves proportional to $\exp(-t_0 f)$, where $t_0 = 0.5$ s and $\exp(-t_0 f)+0.01\exp(-t_1 f)$, where $t_1 = 1/30$ s are shown of comparison. See text.

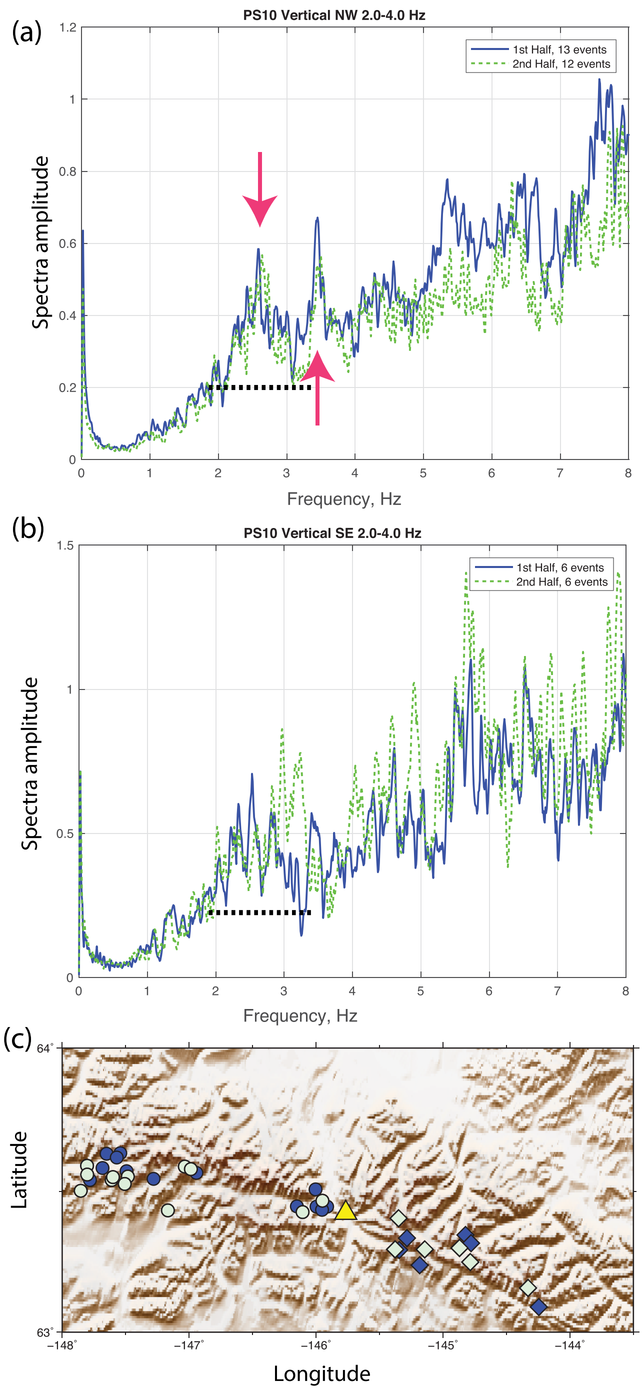

Figure 7. Stacked spectra for Denali aftershocks (Table 2). Spectra amplitude is in arbitrary units. The plotted amplitudes are consistent between panel (a) and panel (b). (a) Aftershocks to the WNW. Early bin 1, solid line and later bin 2, dashed line. Arrows indicate centers of peaks at ~2.6 and ~3.5 Hz that moved with time to slightly higher frequencies. The predicted width of the 2.6 Hz resonance is 2Δ. (b) Aftershocks to the ESE. Early bin 3, solid line and later bin 4, dashed line. The earlier stack resolves the ~2.6 Hz peak, but the latter stack does not. (c) Location map: Triangle; PS10-C; dark circles, bin 1; light circles, bin 2; dark diamonds, bin 3; and light diamonds, bin 4. The aftershocks and the topography crudely show the Denali Fault trace.

little to cause instrumental coupling with the vertical signal. Thus, local site resonance from lateral heterogeneities (Anooshehpoor & Brune, 1989; Sleep, 2012) likely entangled signal from the strong vertical component into the weaker horizontal components. The N43.3 W component is naturally oriented to be weakly coupled with the vertical component through laterally heterogeneous structure. Note that the Denali Fault strikes approximating west-northwest near PS10 and that PS10 was ~3 km from the fault (see Figure 7c). The radial (propagation) direction for signal arriving from the nearest (~3 km) fault was crudely north-northeast. The radial direction for more distant signal was crudely west-northwest or east-southeast.

The near-field velocity pulse dominates the spectra during its arrival from 16 to 26.24 s (Figure 6b). The dominant frequencies are lower than the ~1.2 Hz resonance for *S* waves. This resonance and the ~4.8 Hz resonance for *P* waves are not evident. In principle, one could predict the velocity pulse at PS10 from records at other stations and then spectrally divide the observation by the prediction. Seismic stations were far too sparse in 2002 near PS10 for this method to be productive (Ellsworth et al., 2004).

Intuitively, inelastic deformation within the gravel caused damage that reduced its seismic velocities. Observation of transient increases of the seismic velocity within the gravel after the strong shaking ceased would indicate that the damage did previously occur and it had begun to heal. Spectra from 30 to 40.24 s interval after the *P* wave and the 40.24 to 50.48 s after the *P* wave are relevant of observing healing of the gravel (Figure 8). The vertical component resolves ~4.8 Hz resonant frequency only during the 0 to 10.24 s before strong shaking and the 40.24 to 50.48 s after strong shaking. The resonant frequency after strong shaking was ~0.5 Hz lower than before the strong shaking. The observation is compatible with the inference that the gravel was damaged. This component, however, does not resolve the resonance between 30 and 40.24 s. Healing between this interval and the 40.24 to 50.48 s interval was thus not resolved.

Physically, observable coupling of the vertical component into the N46.7E component at times of strong *P* waves and weak *S* waves implies coupling of the N46.7E component into the vertical component at times of strong *S*. In addition, the signal is overall weak between 2 and 8 Hz and 30 and 40.24 s. The ~4.8 Hz resonant frequency between 40.24 and 50.48 s of the N46.7E component behaves similarly to the vertical component, giving additional support to the inference that the *P* resonance frequency did change.

The N43.3 W component may marginally show healing of the *S*-wave velocity. The peak of the ~1.2 Hz resonance may shift to lower frequencies from the 0 to 10.24 s interval before strong shaking to the 30 to 40.24 s interval after strong shaking. The resonant frequency may increase toward 1.2 Hz from the 30 to 40.24 s interval to the 40.24 to 50.48 s interval. The N46.7E component does not resolve the 1.2 Hz resonance before the near-field velocity pulse. This component does poorly resolve this resonance after the near-field pulse. A greater proportion of the signal is *S* waves at this time.

The spectra from 40.24 to 81.20 s (near the end of the available record) did not provide more detail. The vertical component was only about 1/3 of the horizontal components. Its spectral peak at ~4.5 Hz was similar to that between 40.24 and 50.48 s but not well resolved. This component showed also the ~1.2 Hz peak that was also present on both horizontal components. By this time interval, P waves apparently no longer dominated the vertical signal.

5. Deep Nonlinearity Associated With the Near-Field Velocity Pulse

The near-field velocity pulse likely caused frictional failure within the stiff crystalline rock beneath the gravel at PS10. We discuss this previously described process (Sleep, 2016 and references therein). Such nonlinearity is a general feature of three-dimensional numerical models of earthquake rupture (Roten et al., 2014, 2016; Roten, Olsen, Cui, & Day, 2017; Wang et al., 2019). There is thus some presumption that this process occurred beneath PS10.

Basically, the strong dynamic stresses and strains associated with the near-field velocity pulse brought the uppermost ~2 km of the crystalline rock to inelastic failure and caused damage. We concentrate phenomenologically on the hypothesis that high-frequency S waves passing through the inelastically deforming region also nonlinearly attenuated. We discuss the effective rheology in section 7. We also use the ambient velocity structure in Figure 2 for paleoseismology to infer peak ground velocities from past major earthquakes before 2002 near PS10.

Our scaling relationships are based on simple kinematics, as there is not enough information for PS10 to formulate a more sophisticated approach. The particle velocity V_{pulse} and displacement within the crystalline rock are mainly horizontal, and the wave of the near-field velocity pulse propagates in the horizontal fault-parallel direction with phase velocity c_{pulse}. At failure, the dynamic stress (horizontal shear traction on vertical planes) in (2) equals the failure stress in (7):

$$\tau_{\text{fail}} = P_{\text{eff}}\mu \approx \mu(\rho - \rho_w)gz = \tau_{\text{dyn}} = G\varepsilon_{\text{pulse}} = \frac{GV_{\text{part}}}{c_{\text{pulse}}}. \tag{10}$$

This equation indicates a criterion for the onset of inelastic failure. The effective value of the shear modulus likely decreased once failure is underway, although we did not resolve this effect.

In a repeatedly shaken region like around PS10, rock damage during each event reduces the shear modulus. In this testable hypothesis, a self-organized process called low-cycle fatigue (Lubliner, 1990) ensues where the shear modulus as a function of depth adjusts so that the strain for failure equals the dynamic strain in typical large events:

$$\varepsilon_{\text{fail}} = \frac{P_{\text{eff}}\mu}{G} = \frac{V_{\text{part}}}{c_{\text{pulse}}} \approx \frac{\mu(\rho - \rho_w)gz}{G}. \tag{11}$$

It should be remembered in terms of (5) that μ may represent a Coulomb stress ratio where the inelastic strain rate goes from slow to fast rather than a sharp coefficient of friction. The key assumptions are (1) the near-field velocity pulse had long enough wavelength that the particle velocities did not change a lot with depth in the uppermost ~2 km. The measured particle velocity at the surface is thus an acceptable approximation for the one at depth. (2) The effective phase velocity was essentially horizontal, at the rupture velocity, and parallel to the fault trace. As discussed in subsection 5.1, published models of the Denali earthquake are insufficient to appraise these assumptions in detail. Generic numerical models of the 1992 Landers earthquake do show development of a nonlinear flower structure along the fault (Roten, Olsen, & Day, 2017).

The right-hand approximate equality in (11) applies when the (preindustrial for the past earthquakes) water table is at the surface and the coefficient of friction and density are constant with depth. Solving for G in terms of constant imposed past dynamic strain $\varepsilon_{\text{fail}}$, the shear modulus increases linearly with depth. Otherwise, finite water-table depth and variations in the coefficient of friction cause predictable variations of G/z from a constant that are observed (Sleep, 2016).

5.1. Dynamic Strains for Crystalline Rock Failure Beneath PS10

We appraise the hypothesis in (11) using Table 1 and Figure 2, which gives the failure strain at the center of each layer for the tabulated density and shear modulus, the water table at the surface as approximately observed, and a coefficient of friction with the generic value of 0.7 (i.e., we assume that many weak cracks, rather than strong intact rock, accommodated the modest inelastic strains).

The centers of the tabulated layers within the crystalline rock in Figure 2 are an approximation for a smooth gradient. The smooth curve through the centers is likely a better representation of the subsurface than the layers. We also modified the solid curve within the gravel and uppermost crystalline rock to include more detailed information from Figure 18 of Kayen et al. (2004).

The computed failure strains are at the centers of the layers that represent the slowly varying failure strains within the velocity gradient in the crystalline rock. We evaluate the scaling relationship in (11) at the centers of the layers where the gradient model and the layered model give the same result. For context from subsection 2.1, the actual dynamic strain was crudely 0.5×10^{-3}. The failure strain at the top of the crystalline rock is 0.35×10^{-3} in the gradient model at an S velocity of ~850 m s^{-1}. The computed failure strains in the centers of upper 3 crystalline rock layers are between 0.45×10^{-3} and 0.7×10^{-3}, that is, crudely ~0.6×10^{-3}. The failure strain at 1700 m depth in the deep crystalline rock also is of ~0.6×10^{-3}, which in Figure 2 is drawn as the base of the damage zone. That is, the calculation indicates that an inelastic strain of ~0.6×10^{-3} will commence damage in the deeper crystalline rock, and a somewhat lower dynamic strain will damage the shallowest crystalline rock. That is, we predict that the shallower crystalline rock preferentially failed from the near-field velocity pulse, but we have no good way to appraise this detail with tomography.

With regard to paleoseismology in (11), the tabulated and plotted data indicate that previous strong near-field velocity pulses of ~0.6×10^{-3} dynamic strain could have repeatedly brought the crystalline rock down to ~1700 m into frictional failure. This value ~0.6×10^{-3} applies to dynamic strain from past Denali earthquakes and is within resolution value of ~0.5×10^{-3} inferred in subsection 2.1 and this subsection for the 2002 Denali mainshock.

We discuss dynamic strains within the gravel in terms of (11) with the caveat that vertically propagating S waves in Figure 3 may be a better approximation. The S-wave velocity at the center of the gravel is ~550 m s^{-1} from Figure 18 of Kayen et al. (2004) rather than 400 m s^{-1} in Table 1. The tabulated failure strain from (11) is $(400/550)^2$ times the tabulated strain of ~1.045×10^{-3} or 0.55×10^{-3}. The S-wave velocity is ~300 m s^{-1} in the uppermost 30 m; the rounded failure strain of 0.6×10^{-3} causes failure at ~18 m depth. The shear modulus in (11) cannot go all the way to zero at very shallow depths. That is, the S-wave velocity and shear modulus in the gravel are crudely self-organized in (11) so that failure occurs at a strain of ~0.6×10^{-3}, as in the crystalline rock.

The lack of observable resonances during the near-field velocity pulse might be attributed to transient failure in the uppermost crystalline rock. A dynamic strain of ~0.35×10^{-3} brings the uppermost crystalline rock into failure. This failure strain is less than that for the base of the gravel and that for the underlying crystalline rock. Preferential failure of the uppermost crystalline rock under the imposed dynamic strain decreases the S-wave velocity of this rock, while the overlying lowermost gravel is not damaged. The reflection coefficient from the gravel-rock interface decreases, and thus the strength of the resonance within the gravel layer decreases. This effect alone does not affect the period of the resonance. The predicted resonance remains weak until the damage in the uppermost crystalline rock heals.

In general, this nonlinear interaction effect may lead to overall weakening of the reverberating surface signal and hence reduce peak ground acceleration. Traditional site response formalism includes strengthening of the resonance from damage in the shallow layer but not weakening of the resonance from damage to the top of the underlying crystalline rock. In addition, the deeper damage is associated with long-period waves, which here are associated with the near-field velocity pulse. We are not aware of a published treatment of this nonlinear effect. We note that receiver function methods (e.g., Tao et al., 2014) might be able to monitor transient changes in the reflection coefficient at the base of the gravel and seismic velocity changes within the gravel associated with healing. We discuss relevant digital aftershock data in section 6.

We continue by comparing the observed dynamic strain in the Denali earthquake at PS10 with this predicted failure strain of ~0.6×10^{-3} using (2). A PGV velocity of 1.8 m s^{-1} was measured. We begin with the generic value of 3.5 m s^{-1} for rupture velocity in an example, which yields a dynamic strain of 0.52×10^{-3}. This value is close (within resolution) to the predicted failure strain of 0.6×10^{-3}. We now examine constraints of the dynamic velocity within the crystalline rock and appropriate value of the propagation velocity.

The long-period dynamic velocity in the crystalline rock differed somewhat from the measured value at the surface. There were only mild reverberation effects, as the frequency of most of the near-field velocity pulse was below the resonant frequency ~1.2 Hz for *S* waves in the gravel (Figure 6b). However, the significant nonlinearity in the gravel kinematically implies that PGV in the crystalline rock was somewhat greater than that at the surface. In this hypothesis, nonlinear attenuation in the gravel clipped acceleration (Figures 3 and 4), so the surface velocity increased more slowly with time than at depth. A somewhat longer duration for the surface dynamic velocity is integrated to give the essentially same dynamic displacement, as did a somewhat shorter interval of higher dynamic velocity in the crystalline rock.

5.2. Rupture Velocity Beneath PS10

The rupture velocity (or phase velocity) beneath PS10 in (11) was somewhere around the *S* velocity of the deep rocks, but it is difficult to do better. Published inversions for slip during the Denali earthquake do not agree, and as already noted, it is not possible to infer the details of rupture near PS10 independently of the PS10 records. Asano et al. (2005) give ~3.5 m s^{-1} near PS10. Dreger et al. (2003) give the range of 3.3–3.7 m s^{-1}. Frankel (2004) and Liao and Huang (2007) used 3.5 m s^{-1} for modeling. Oglesby et al. (2004) limited the rupture velocities to 3.3 m s^{-1} for dynamic modeling. Walker and Shearer (2009) obtained 3.3 m s^{-1} using a back projection method.

Ellsworth et al. (2004) and Dunham and Archuleta (2004) obtained the supershear velocity of ~5.5 m s^{-1} from the waveforms at PS10. They inferred that only a short segment of the fault west of PS10 became supershear. The back projection method of Walker and Shearer (2009) did not resolve this feature. Frankel (2004) also did not resolve supershear rupture on this segment. He did resolve a subevent near PS10 that was delayed after the nominal rupture front. The complicated signal from the subevent, if real, might mimic supershear effects on the PS10 records. It also complicates inference of peak dynamic strain beneath PS10.

5.3. Additional Preearthquake Ambient Stresses and Elastic Strains

An additional complication is that the near-field velocity pulse augments the static shear traction that built up around the fault since the previous large event. Overall, the dynamic shear traction tends to align somewhat with the static shear traction to cause failure. Published dynamic and static models of the Denali event provide neither tensor dynamic strain nor tensor coseismic static strain beneath PS10. There is no simple way to extract this information from the models. There was no INSAR coverage near PS10 (Wright et al., 2004); so the static coseismic strain at PS10 and the local depth of rupture are poorly constrained.

Static stress drops from models of the earthquake do constrain static strain with poor resolution. Dreger et al. (2004) gave range of between 1.3 and 5.0 MPa. Wesson and Boyd (2007) gave 1–4 MPa. Aftershocks show that the stress drop was nearly total (Ratchkovski, 2003; Wesson and Boyd, 2006). For example, the static strain for 4 MPa stress drop and the deep shear modulus of 30 GPa in Table 1 is 0.13×10^{-3}. This value is a modest part of the computed dynamic strain of 0.52×10^{-3}, but again detailed information is not available for PS10.

5.4. Search for Suppression of *S* Waves by the Near-Field Velocity Pulse

It is obvious that the high-frequency *S* waves recorded at PS10 were relatively weak (Ellsworth et al., 2004; Martirosyan et al., 2004). The resolved normalized horizontal acceleration was barely above 0.1 except during the near-field velocity pulse (Figures 4 and 5). The high-frequency signal is also isotropic in the sense that oscillations fill the 0.1 g circle about the origin. These are the key observations that we use to infer that the near-field velocity pulse did suppress *S* waves.

We point out alternative hypotheses: (1) An effective coefficient of friction of ~0.1 would explain this observation in (9). However, this very low value seems unlikely for gravel and crystalline rock. One would then need another explanation of why the near-field velocity pulse clipped at ~0.35 g and yielded the reasonable effective coefficient for gravel of 0.35, which is well above 0.1. (2) It is conceivable that the Denali earthquake did not generate strong high-frequency *S* waves to begin with or that high-frequency signal was trapped within the fault zone so that no deep nonlinear attenuation is needed. We have only raw spectra, so we cannot a priori dismiss source effects, effects from the velocity structure near the fault plane, or even very shallow effects. We begin with high-frequency *S* waves during the near-field velocity pulse and then examine differences between spectra before and after this strong shaking.

In more detail, the dynamic stress from the near-field pulse and hence nonlinear attenuation of the high frequency waves is likely to vary along a ray path (or ray tube). We begin with pseudolinear attenuation where observed horizontal spectra do decay as

$$\exp(-t_0 f) = \exp(-\omega t_0/2\pi) = \exp\left(-\pi f \kappa_{\text{path}}\right) = \exp(-\omega f t/2Q), \tag{12}$$

where f is frequency, t_0 is an empirical factor with dimensions of time, ω is angular frequency, and the factor κ_{path} is used in geotechnical studies to represent attenuation (e.g., Hassani & Atkinson, 2018), which is convenient in this paragraph. The final equality uses the effective quality factor Q over the travel time t of the ray path. The factor κ_s over each segment s of the ray path decreases the predicted amplitude by the factor $\exp(-\pi f \kappa_s)$. The net attenuation factor is the product of (or integral over) the effect of each segment $\prod_s \exp(-\pi \kappa_s f) = \exp\left(-\pi \kappa_{\text{path}} f\right)$, where $\kappa_{\text{path}} \equiv \sum_s \kappa_s$. Finally, the actual predicted signal is the sum of (or integral over) numerous rays that experienced different net attenuations. It might be possible to do time-dependent and frequency-dependent tomography with a dense network of near-fault stations, but we have only the single PS10 record for the Denali mainshock.

The observed horizontal spectra during the near-field velocity pulse in Figure 6b decay exponentially with frequency with $t_0 \approx 0.5$ s. A simple explanation is that the apparent quality factor Q in (12) does not depend strongly on frequency and that the initial spectra of high-frequency *S* waves were initially flat as expected, from the well-known scaling of displacement spectra to ω^{-2} above the corner frequency. Here, we suspect strong transient attenuation along part of the deep path through near-field pulse where the linear apparent attenuation $1/Q$ and effective propagation time t are not known a priori. We use 3 s for an example with the inference that the *S* waves and the near-field pulse propagated together, so the effective time is longer than the duration for a near-field pulse at fixed station PS10. The effective quality factor Q in (12) is thus ~20, implying that the shear waves were significantly damped.

The high-frequency tails of the spectra provide additional information (Figure 6c). A small amount of the horizontal signal either seems to have evaded the near-field velocity pulse as *S* waves or was converted from *P* waves. In general, the recorded signal is the sum of the effects of numerous ray paths that experienced different attenuations. This slowly attenuating signal becomes evident only at high frequencies; proportional to $\exp(-\omega t_0/2\pi)+0.01\exp(-\omega t_1/2\pi)$, where $t_1 = 1/30$ s provides a better fit. The apparent Q associated with t_1 is ~15 times that associated with t_0 or ~300. For calibration, the linear low-amplitude shear wave Q is 100 in the gravel and 200 in the crystalline rock; the linear low-amplitude *P*-wave Q is 200 in the gravel and 400 in the crystalline rock (Frankel, 2004). Adjusting the propagation time from 3 to 2 s gives an apparent *S*-wave Q associated with t_1 of 200 in agreement with Frankel's (2004) value for the crystalline rock.

The survival of high-frequency *S* waves of modest amplitude at the tail of the spectrum indicates that the earthquake source generated some of these waves at the time of the near-field velocity pulse. It also indicates that these waves were able to transmit through the shallow gravel. The apparent Q of the high-frequency tail is similar to the low-amplitude value 200 inferred by Frankel (2004) and hence compatible with the expected Q of ray paths that evaded the near-field pulse. This apparent Q is much greater than 20 the (pseudolinear) apparent value for most of the *S*-wave signal during near-field velocity pulse.

Signal from early and from late in the record bears on source and gravel properties. *S* waves generated west of PS10 from 0 to 10.24 s moved more or less with the near-field velocity pulse and hence potentially experienced nonlinear attenuation along much of their paths. However, the source was able to generate some high frequency both late and early in the record. By 40.24 to 50.48 s, the rupture front had moved well to the east, so there is some expectation that the near-field velocity pulse no longer was available to strongly suppress *S* waves that propagated in the opposite direction. The N43.3 W component was less coupled with *P* waves and hence a more reliable indicator of nonlinear attenuation of high-frequency *S* waves than the N46.7E component. From 0 to 10.24 s, the higher-frequency amplitudes for N43.3 W were lower than the 1.2 Hz peak. Amplitudes were somewhat elevated between 6 and 8 Hz. The vertical amplitudes were also strong in this interval, so coupling of *P* waves into the horizontal component is conceivable. Still, the presence of high-frequency *P* waves is an indication that the source could generate high-frequency *S* waves. From 40.24 to 50.48 s, 2–7 Hz high-frequency horizontal signal was comparable to the ~1.2 Hz resonance. The persistence of high-frequency horizontal signal is an evidence that nonlinear attenuation along the ray paths had waned by this time. Strong ordinary linear attenuation within the gravel with $Q \approx 20$ would be expected to preferentially suppress the high-frequency signal relative to the resonant signal. We inferred that nonlinear attenuation associated with the near-field velocity pulse had this effect earlier in the earthquake.

The initial low-amplitude signal is relevant to the source's tendency to generate high-frequency body waves. Physically, local irregularities in fault motion should generate both high-frequency *P* waves and high-frequency *S* waves. Strong high-frequency *P* waves arrived before the near-field velocity pulse (Figure 5). These *P* waves outran the near-field velocity pulse soon after they were generated and thus likely evaded nonlinear attenuation by the pulse. Furthermore, the vertical spectrum of these waves was strong at high frequencies (Figure 6a) and relatively flat up to ~13 Hz. The well-known asymptotic scaling of displacement to ω^{-2} above the corner frequency implies flat acceleration spectra in the absence of attenuation. Ordinary linear attenuation thus did not greatly suppress the *P* waves up to 13 Hz and only mildly to 20 Hz.

However, two difficulties arise explanations that involve apparently constant low Q for *S* waves: (1) Nonlinear inelastic rheology (including plastic rheology) in (3) does not exponentially suppress high-frequency waves. That is, the predicted quality factor from (3) Q in (12) is then dependent on frequency. (2) The horizontal high-frequency signal in Figures 8a and 8b from 30 to 40.24 s remained weak even though the near-field velocity pulse had moved on. We return to these topics in section 7.

5.5. Adjustment of Estimate of Deep Particle Velocity

A related kinematic effect is that rock failure diminished the near-field velocity pulse. This effect was likely moderate. Most of the energy in the pulse had recorded frequencies lower than 1 Hz, where the signal was damped by a factor of ~3/4 extrapolating the exponential curve (Figure 6b). Nonlinear attenuation reduced the particle velocity at the surface relative to that at depth. For reference, multiplying by 4/3 to restore the 1.8 m s^{-1} amplitude yields 2.4 m s^{-1} and 0.69×10^{-3} dynamic strain beneath the attenuating zone in the crystalline rock. This mild adjustment is compatible with the inference that inelastic strain only modestly reduced the amplitude of the near-field velocity pulse. The inferred maximum depth to failure was factor of ~4/3 greater than the 1700 m depth inferred above. We use the rounded failure depth 2000 m in further discussions to avoid spurious precession.

Kinematically, the time integral of velocity needs to yield the static displacement both at the surface and beneath the zone of failure. If the deep and shallow displacements are the same, a longer duration modestly reduced velocities at the surface equaled that a shorter duration of somewhat higher velocities at depth. However, there may have also been some shallow slip deficit (Kaneko & Fialko, 2011; Roten, Olsen, & Day, 2017). In that case, the product of particle velocity at depth with its duration exceeded this product at the surface. Therefore, the deep particle velocity of 2.4 m s^{-1} inferred above may be also modestly underestimated by a factor related to the shallow slip deficit.

5.6. Comparison With the Lucerne Record From the 1992 Landers Earthquake

We provide another field example to aid in understanding the underlying physics. High-frequency *S* waves impinged on Lucerne (LUC, located at 34.568°N, 116.612°W) during the 28 June 1992 Landers M_w 7.2 earthquake. As with PS10, this station was close ~1.25 km to the main fault rupture. Sleep and Nakata (2015) noted that the near-field velocity pulse may have suppressed *S* waves. Three-dimensional nonlinear numerical models (Roten, Olsen, Cui, & Day, 2017) of the Landers earthquake show failure with a flower structure with shallow nonlinear attenuation away from the fault, which supports this inference.

Chen (1995) and Iwan and Chen (1995) obtained corrected digital seismograms from the analog record. Horizontal PGV was 1.5 m s^{-1}, similar to 1.8 m s^{-1} recorded at PS10 during the Denali earthquake. Unlike PS10, LUC recorded strong high-frequency *P* waves and *S* waves with accelerations up to ~0.8 g. The issues of this earthquake not generating any strong high-frequency waves or these waves being unable to ever reach

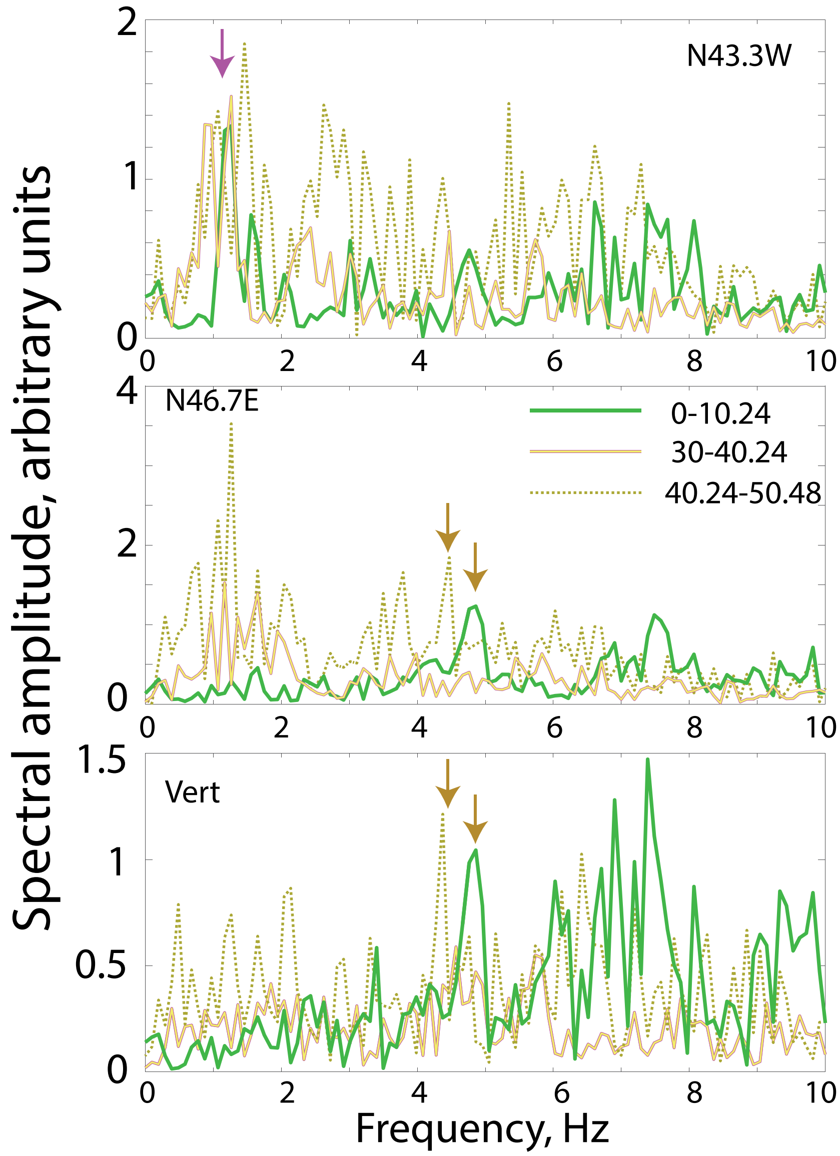

Figure 8. Spectral acceleration amplitudes for the N43.3 W, N46.7E, and vertical components for the intervals 0–10.24, 30–40.48, and 40.24–50.48 s show expected effects of gravel damage from strong shaking. On all the panels, the 0–10.24 record's gain is increased by a factor of 7 and the 40.24– 50.48 gain by a factor of 3 relative to the 30–40.24 interval so that the amplitudes of the ~1.2 Hz peaks on the N43.3 W panel are similar at all times. The suspected S-wave resonance at 1.2 Hz moved to lower frequencies from 30 to 40.24 s on the N43.3 W component. It recovered toward its initial value from 40.24 to 50.48 s. The suspected P-wave resonance at 4.8 Hz moved to lower values from 40.24 to 50.48 s on the vertical and N46.7E components..

the station do not arise. The rupture jumped between different fault segments (e.g., Wald and Heaten, 1994). The irregularities in the fault trace are conceivable sources of high-frequency signal.

The high-frequency horizontal acceleration was weak, while the initial part of the near-field velocity pulse passed (Sleep & Nakata, 2015), as it was at PS10 (Figure 9). High accelerations occurred later. The main differences of LUC with the PS10 record are that longer-period dynamic accelerations were weak for most of the near-field velocity pulse at PS10. High-frequency oscillations at LUC were centered at the origin between 7 and 8.5 s and about 0.2 g, somewhat greater that the high-frequency accelerations at PS10. A stronger sustained long-period dynamic acceleration of ~0.17 g arrived between 8.5 and 8.875 s. The circle of oscillations moved ~0.17 g to the west, and the amplitude relative to the center of this circle was similar to that in the prior interval, 0.2 g. That is, the high-frequency *S*-wave motion directions were isotropic as at PS10.

That is, nonlinear suppression of S waves by the near-field velocity pulse is reasonable beneath LUC, but the resulting acceleration was greater than that at PS10. Modest high-frequency accelerations from S waves coexist with the near-field velocity pulse and appear to behave additively in Figure 9b. The duration of reduced high-frequency signal at LUC was much briefer than that at PS10. We return to this topic in section 7.

6. Search for Healing of the Gravel and of the Crystalline Rock

We appraise the hypothesis that strong seismic waves damaged the gravel and crystalline rock beneath PS10 by looking for subsequent increases of seismic velocities from healing after the mainshock. We concentrate on transient changes in seismic velocity and make no attempt to improve models of the absolute seismic velocities by Brocher et al. (2004), Frankel (2004), and Kayen et al. (2004). Aftershock data recorded by Carver et al. (2003) are suitable for this purpose. Their temporary stations near PS10 were not installed until 7 days after the mainshock and continued to record until 20 days after the mainshock. We present results with at best marginal resolution to illustrate approaches that may be applicable to future well-recorded earthquakes.

We study data collected by Carver et al. (2003) from their temporary PS10 (latitude = 63.4237°N, longitude = −145.7660°E) that was within a plywood-sided structure and ~50 m from PS10. This station collected signals from aftershocks located by Carver et al. (2003) from 9 November to 15 November 2002 (Table 2). We hereafter refer to this station with our own designation of PS10-C to avoid confusion with the mainshock station PS10.

The Kinemetrics K2 Instruments with Episensor accelerometers at PS10-C have flat spectral response from DC to the Nyquist frequency of 50 Hz. The instruments operated in triggered mode. We are thus unable to apply ambient noise passive seismology. In addition, we cross-correlated the P-wave arrivals of all recorded events at PS10-C but were unable to find any repeating events. We were unable to locate any aftershock data from PS10 itself. We also obtained data from nearby crystalline rock sites in the temporary array, which we do not present here.

Studying healing of the gravel is in principle straightforward, as one can traditionally monitor its resonance frequencies. We apply receiver functions to monitor the change in the reflection coefficient at the base of the gravel associated with healing of damage in the uppermost crystalline rock. However, we do not have a definitive way to associate spectral peaks with ray paths.

6.1. Search for Transient Changes in the Seismic Velocity of the Gravel

We investigate healing of the gravel layer using the spectral peak on the vertical component that is likely associated with reverberating P waves. The stations are ~50 m apart, so we cannot be sure that the thicknesses and seismic properties of the gravel are the same in both locations. Detecting any difference between the resonant frequency from 40.24 to 50.48 s in the aftermath of the mainshock at PS10 and the resonant frequency days later at PS10-C is here of limited value. We thus examine changes between earlier and later aftershocks. For plausibility of our approach, Han et al. (2015) resolved vertical resonant frequency changes in gravel after large events in Japan.

Still, the vertical resonance at PS10 of ~5 Hz indicates where to look for vertical resonance at PS10-C. We also present the expected width of the resonance for a layer over a half-space for future reference. The full width is

$$2\Delta = 2(t_A\pi)^{-1}, \tag{13a}$$

where the amplitude retention time is

$$t_A = \left(\frac{4\rho_g Z_g}{\rho_H \alpha_H}\right)\left(\frac{2\rho_g \alpha_g}{\rho_H \alpha_H + \rho_g \alpha_g}\right)^{-2}, \tag{13b}$$

where Z_g is the thickness of the gravel, ρ is density, α is P-wave velocity, and the subscripts g and H indicate gravel and half-space. We present an example from Table 1, calibrated to give a 2.6 Hz resonance

Table 2
Denali Aftershocks

Number	Date	Time	Longitude, °E	Latitude, °N	Magnitude
Bin 1					Mean = 3.76
1NW	2002-11-09	05:17:38.72	−147.542	63.634	3.8
2NW	2002-11-09	06:45:47.16	−147.781	63.540	3.7
3NW	2002-11-09	08:39:06.38	−145.913	63.446	3.1
4NW	2002-11-09	10:00:00.89	−147.650	63.632	4.5
5NW	2002-11-09	11:03:13.43	−147.493	63.571	4.8
6NW	2002-11-09	14:41:42.67	−146.151	63.447	3.2
7NW	2002-11-09	16:36:04.92	−147.570	63.619	4.1
8NW	2002-11-09	17:14:15.38	−145.996	63.446	3.6
9NW	2002-11-09	20:19:47.43	−145.953	63.435	2.7
10NW	2002-11-11	18:40:27.82	−146.004	63.507	3.3
11NW	2002-11-11	19:13:09.82	−146.943	63.565	3.9
12NW	2002-11-11	20:09:53.31	−147.280	63.544	4.0
13NW	2002-11-11	20:31:11.91	−147.682	63.582	4.2
Bin 2					Mean = 4.08
14NW	2002-11-11	22:07:56.85	−147.804	63.590	4.1
15NW	2002-11-12	09:28:17.09	−147.034	63.587	3.6
16NW	2002-11-12	13:34:08.00	−145.950	63.467	4.0
17NW	2002-11-13	04:09:05.43	−147.483	63.552	3.9
18NW	2002-11-13	08:39:14.90	−146.986	63.578	4.1
19NW	2002-11-14	03:09:40.87	−147.610	63.540	4.1
20NW	2002-11-14	14:37:23.76	−146.106	63.427	5.1
21NW	2002-11-14	16:57:24.36	−147.507	63.526	3.7
22NW	2002-11-14	21:24:57.81	−147.854	63.502	3.9
23NW	2002-11-15	05:23:56.00	−147.167	63.433	4.3
24NW	2002-11-15	08:15:31.00	−147.600	63.550	4.2
25NW	2002-11-16	01:20:12.18	−147.803	63.559	3.9
Bin 3					Mean = 3.70
1SE	2002-11-09	03:03:42.61	−144.245	63.090	4.2
2SE	2002-11-09	07:44:24.52	−145.184	63.239	3.7
3SE	2002-11-11	17:29:58.71	−145.345	63.293	2.7
4SE	2002-11-11	22:27:21.45	−145.284	63.335	3.4
5SE	2002-11-12	00:24:16.12	−144.823	63.346	4.5
6SE	2002-11-12	00:24:16.12	−144.779	63.317	3.7
Bin 4					Mean = 3.70
1SE	2002-11-12	06:26:41.48	−144.870	63.300	3.5
2SE	2002-11-12	06:43:40.57	−145.350	63.405	3.6
3SE	2002-11-13	06:43:40.57	−145.377	63.295	2.8
4SE	2002-11-13	13:40:39.04	−144.330	63.158	5.1
5SE	2002-11-15	18:37:28.52	−145.144	63.295	3.7
6SE	2002-11-15	18:53:31.84	−144.785	63.250	3.5

Data from Carver et al. (2003). Mean magnitude is given for each bin.

peak with forethought. The gravel is 173 m thick; its density is 1800 kg m^{-3}, and its *P*-wave velocity is 1800 m s^{-1}. The density of the half-space is 2400 kg m^{-3}, and its *P*-wave velocity is 2500 m s^{-1}. The calculated resonance width is 1.5 Hz.

The apparent coupling for the horizontal N46.7E component with the vertical component at PS10 indicates that there may also have been directional site effects at PS10-C. Crystalline rocks outcrop east and south of PS10-C (Carver et al., 2003). It might be expected that the base of the gravel is not horizontal and might thicken to the west. The aftershocks are near the Denali Fault and hence ~WNW or ~ESE of PS10-C. We sorted aftershocks located by Carver et al. (2003) into those back azimuths (Figure 7 and Table 2). We did not use unlocated events, although the recorded motion of the initial *P* wave does constrain the back azimuth to some extent. We sorted the located events into four bins with two time intervals and WNW and ESE back azimuths (Figure 7 and Table 2). Magnitudes range from 2.7 to 5.1 (Carver et al., 2003).

10.1029/2019JB018386

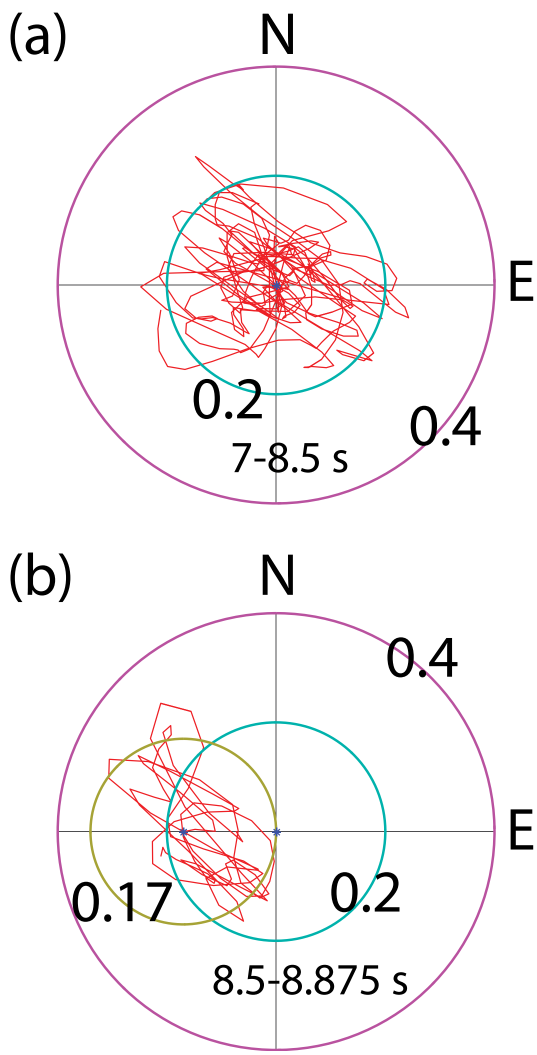

Figure 9. Polar plot of dynamic acceleration recorded at LUC as in Figure 2. (a) From 7 to 8.5 s the long-period acceleration from the near-field velocity pulse was weak. High-frequency motion was centered at the origin and less than ˜0.2 g. 47 (b) Between 8.5 and 8.875 s, the long-period acceleration was ˜0.17 g to the west. High-frequency oscillation is centered to 48 ˜0.17 g west of the origin. The amplitudes measured from this center are approximately similar to 0.2 g to those measured 49 from the origin in panel (a).

We computed vertical spectra using the full available record for each aftershock after removing linear trends and tapering the data. The number of time data points and hence the computed frequencies differed for each aftershock. We interpolated to 0.01 Hz in frequency prior to stacking. We normalized each spectrum with the peak amplitude in the range 2–4 Hz before stacking so that each aftershock makes a similar contribution in the frequency range of the initial interest.

With regard to impinging signal, the expected acceleration spectrum of each event is crudely flat above the corner frequency and proportional to ω^2 below the corner frequency. The stacked spectra had a range of magnitudes and hence a range of corner frequencies (Figure 9 and Table 2). The corner frequency of the larger events was around 5 Hz; the normalized spectral amplitude of these events did not increase much above 5 Hz. The corner frequency of the smaller events was well above 5 Hz; the normalized spectral amplitude of these events increased above the amplitude at 5 Hz. The events with high corner frequencies dominate the stack at high frequencies.

This normalization procedure achieved the goal in the region of interest that each event contributed similarly to the stacks. The data show that aftershocks did generate high-frequency signal and that (by 7 days after the mainshock) the gravel and crystalline rock beneath PS10-C could efficiently transmit high-frequency low-amplitude signal.

The expected spectra peak near ~5 Hz that was observed for the mainshock at PS10 is not evident for the aftershocks WNW of PS10-C (Figure 9a). There is a peak a ~2.6 Hz. The width of the peak is ~1.5 Hz also as expected. The later broad peak is systematically displaced slightly (0.025–0.05 Hz) toward higher frequencies as would be expected from healing of the *P*-wave velocity in the gravel. A second broad peak is centered at ~3.5 Hz and similarly displaced toward higher frequencies at later times. Undue attention should not be given to the individual narrow peaks. The ESE aftershocks show a broad peak around ~2.6 Hz in the earlier spectrum that is not resolved in the later spectrum.

The cause of the difference between the WNW and ESE spectral stacks is not obvious. There were twice as many aftershocks in the WNW bins, so stacking is expected to better suppress spectral vagaries in the impinging signal. All but 2 of aftershocks in bin 1 occurred on the first day, so there is greater effective time interval between the WNW bins and the ESE bins. It is also conceivable that the site resonances are directional beneath PS10-C.

The ~3.5 Hz peak in the WNW spectra requires some explanation. Kayen et al. (2003) did not report detailed *P*-wave structure near PS10-C, so we make kinematic inferences from their *S*-wave work. For example, it is plausible that the water table was not exactly at the surface at PS10-C. The *P*-wave velocity was then a factor of ~$\sqrt{3}$ of the shallow *S*-wave velocity of 300 m s^{-1} or ~520 m s^{-1}. Dry gravel with thickness of ~13 m above the water table with that velocity and 130 m of gravel with the wet velocity of 1800 m s^{-1} would have a ~2.6 Hz resonance for the full gravel and ~3.46 Hz resonance within the wet gravel. The predicted resonance frequency within the dry gravel is ~10 Hz. The 13 m thickness of the dry gravel is poorly constrained as we have only indirect indications of its *P*-wave velocity.

In addition to the ~10 Hz resonance in the dry gravel, first overtones at ~7.8 and ~10.5 Hz are predicted for the 2.6 and 3.5 Hz resonances. PS10-C recorded strong signal in this frequency range. We normalize each

10.1029/2019JB018386

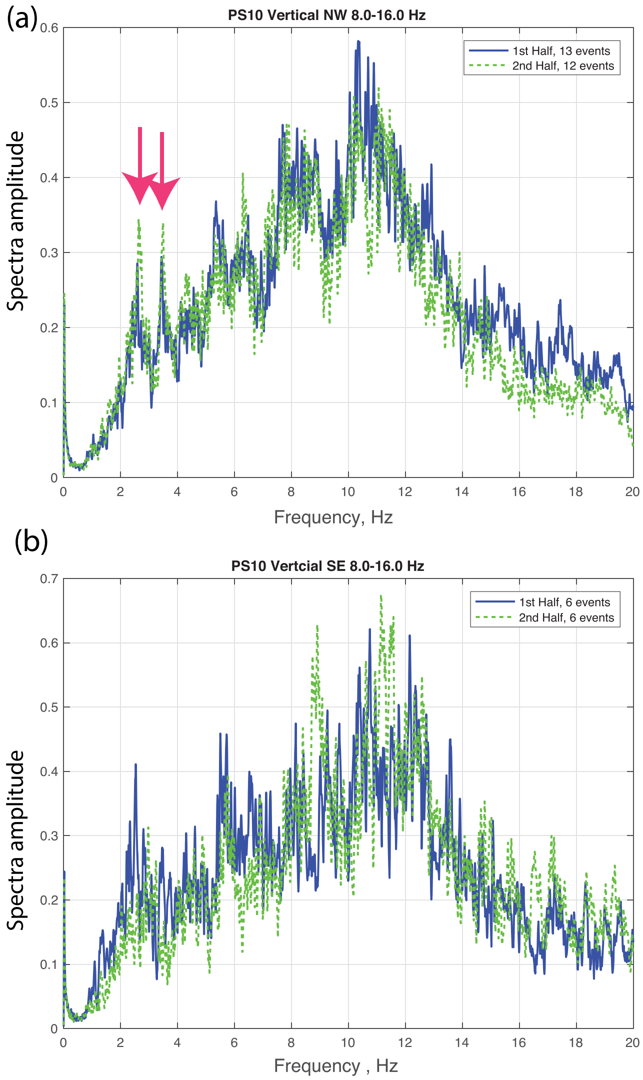

Figure 10. Stacked spectra for Denali aftershocks (Table 2) normalized to the 8 to 16 Hz interval as in Figure 8. (a) Aftershocks to the WNW. Early bin 1, solid line and later bin 2, dashed line. Arrows indicate centers of peaks at ~2.6 and 3.5 Hz that moved with time to slightly higher frequencies. A broad peak is resolved around 11 and 21 Hz. (b) Aftershocks to the ESE. Early bin 3, solid line and later bin 4, dashed line. The earlier stack resolves the ~2.6 Hz peak, but the latter stack does not.

vertical aftershock spectrum to the peak amplitude in the region of interest between 8 and 16 Hz so that each spectrum makes similar contributions to the stack (Figure 10). The ~2.6 and ~3.5 Hz peaks and their slight offset over time are still evident in the WNW stack. This observation hints that the similar behavior in Figure 7 is not an artifact of the weighting method in the stack. Again, the ESE data do not usefully resolve spectral peaks. There is a broad peak in the WNW stack around 11 Hz because ordinary attenuation becomes important at higher frequencies. The predicted higher-frequency peaks are not resolved.

Returning to our main objective, healing is classically expected to progress with the logarithm of time since the mainshock. We provide a simple example. The WNW bins were collected at ~7 and ~12 days after the mainshock. The predicted increase in *P*-wave velocity is thus proportional to $\ln(12/7) = 0.54$. The change since the end of the mainshock depends on the time after strong shaking ended for the measurement from 40.24 to 81.20 s, ~60 s = 7×10^{-4} days. The full predicted increase is proportional to $\ln(10/7\times10^{-4}) = 9.8$, where aftershock data are crudely 10 days after the mainshock. The observed frequency decreased by ~0.25 Hz (~10% of the resonant frequency) from its low-amplitude value at the start of shaking to the immediate aftermath of shaking at PS10. The predicted frequency increase during the aftershock interval is ~0.25 Hz/(9.8/0.54) = 0.014 Hz, which is somewhat less than our estimate from data of 0.025 to 0.05 Hz. There is crude agreement given that strictly logarithmic behavior is assumed over a wide range of time spans. We also do not know if the coseismic decrease in the spectral peak was 0.25 Hz at both PS10 and PS10-C. For reference, Han et al. (2015) observed decreases of the resonant frequency in shallow dry gravel of over 50%. The utility of installing temporary digital seismograms quickly after the mainshock or in this case of keeping the original PS10 operational should be evident.

The stacks of vertical spectra are weak around 1 Hz. We did not resolve the ~1.2 Hz horizontal resonance associated with *S* waves at PS10. The weak signal at this frequency may not even be dominated by *S* waves. We do not attempt further analysis of this peak.

6.2. Search for Transient Changes in the Seismic Velocity of the Uppermost Crystalline Rock

The dynamic strains associated with the near-field velocity pulse in our hypothesis brought the uppermost crystalline rock into nonlinear failure, as discussed in section 5.1. Postseismic increases in the seismic velocities of the crystalline rock would show it was in fact coseismically damaged. We concentrate on methods related to the seismic impedance contrast between the crystalline rock in the gravel, as we have not identified ray paths, which we can time, through the crystalline rock. We do not know a priori whether the crystalline rock actually healed more than the overlying gravel during our observations.

In particular, we use *P*-to-*S* receiver functions at PS10-C. PS10 did not record any strong aftershocks suitable for receiver functions in the available 83.67 s of record after the initial *P* wave. Weak bursts of high-frequency (to the 100 Hz Nyquist) vertical and horizontal signal did occur in the later ~50 s of the record when rupture had moved well to the east. Small immediate aftershocks on the nearby fault plane could well have generated this signal. None of the events was large enough compared with coarriving signal to attempt receiver functions.

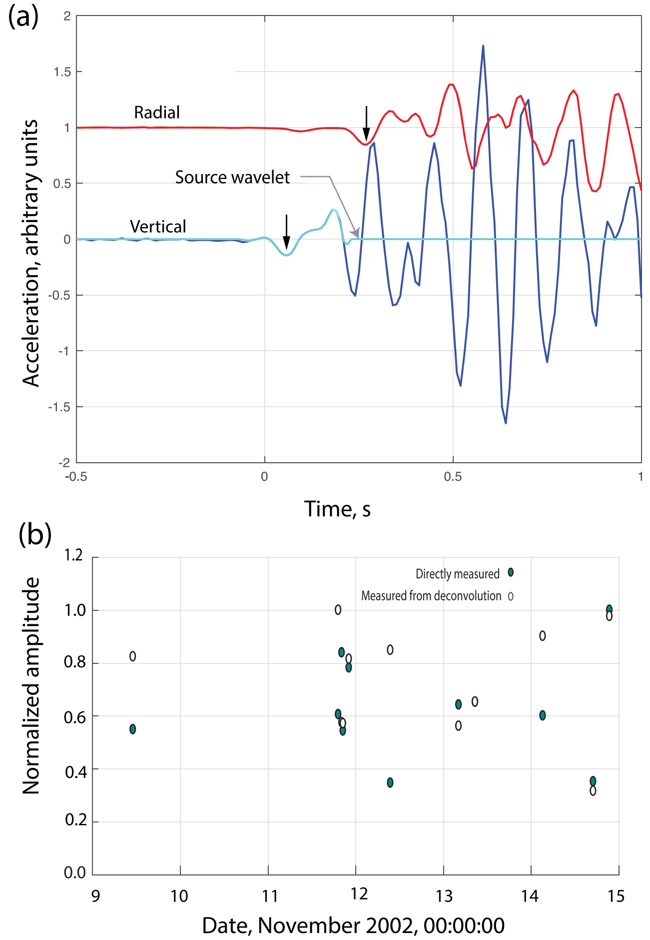

Figure 11. (a) Vertical and radial acceleration records for aftershocks 20NW (Table). We truncated the source wavelet to compute receiver functions. The delay between the vertical peak (arrow) and the radial peak (arrow) is ~0.2 s. We measured the amplitude ratio of these peaks. (b) Radial to vertical amplitude ratios of the aftershocks to the northwest of PS-10 as a function of time. Receiver functions (filled ovals) and direct measurement (open ovals) yielded much scatter and no apparent trend.

We also searched for small very shallow (tens of meters) earthquakes that would generate high-frequency bursts of signal at times of peak dynamic stress (Fischer & Sammis, 2009; Fischer, Peng, et al., 2008; Fischer, Sammis, et al., 2008). Following these works, we high-pass filtered the full time series above 20 Hz. The maximum resolved horizontal amplitude is 0.017 g, which is weak compared to amplitudes of over 0.1 g for known driven shallow events. In addition, further filtering revealed that the high-frequency pulse correlated with in-phase strong broadband arrivals on all three components. These high-frequency pulses are likely to be the high-frequency tails of broadband arrivals with comparable horizontal and vertical amplitudes. Detecting very shallow induced earthquakes would have confirmed the reality of shallow rock failure from strong shaking.

With many more aftershocks, it would be possible to simultaneously invert for seismic structure and for a broad spectrum associated with the effects of corner frequency and attenuation for each aftershock. Conversely, receiver function methods attempt to mathematically suppress the effects of the spectra of impinging waves.

The width of the vertical resonance Δ in (13) and the strength of the spectral peak would, in principle, provide constraints on the crystalline rock velocity. However, the peak width is not precisely resolved in our data. It is also unlikely that the erosional unconformity between crystalline rock and gravel is precisely flat beneath PS10 and PS10C. The interface outcrops in the area of these stations (Carver et al., 2003). For plausibility of lateral heterogeneity, we observe directional site effects with our stacks.

We use *P*-to-*S* receiver functions because the expected *P* arrival for *S*-to-*P* receiver functions coarrives with *P*-wave coda in our data. We begin by estimating the *P*-to-*S* delay for a conversion at the base of the gravel using Figure 7. The *P*-wave resonance is ~2.6 Hz, which implies a 0.0962 s one-way vertical travel time. The *S* resonance was not resolved at PS10-C. However, the *S*-wave resonance of ~1.2 Hz and the *P*-wave resonance of 4.8 Hz at PS10 indicate a *P*-to-*S* velocity ratio of ~4. Applying that ratio, the estimated one-way *S*-wave travel time is 0.3846 s at PS10-C. The predicted delay is 0.3226 s. We instead observe a converted phase with a delay of ~0.2 s (Figure 11a).

We studied aftershocks farther than 50 km away to the WNW of PS10-C so that the impingement points and angles of incidence on the base of the gravel were similar. The initial vertical *P*-wave signal was ringy and lasted much longer than ~0.2 s to the first converted phase (Figure 11a). Traditional *P*-to-*S* receiver function using the full signal provided no useful information. We thus concentrate on the initial signal that is intuitively from the direct *P*-wave. We truncated and tapered that vertical signal to 0.2 s after the start of the *P* wave and then deconvolved this signal with the radial component. We were also able to resolve the amplitude ratio of the converted radial component to the initial *P* wave. We also used the simple method of measuring the ratio of the peak amplitudes of the radial waves to the initial *P* wave. The resulting amplitude ratios had much scatter and no apparent trend that would resolve healing of the uppermost crystalline rock (Figure 11b). We did not attempt any other approach to this task.

7. Discussion and the Rheology of the Crystalline Rock

There is some expectation from generic numerical models of earthquake rupture that brought the crystalline rock beneath PS10 into inelastic failure (Roten et al., 2014, 2016; Roten, Olsen, Cui, & Day, 2017; Wang et al., 2019). In addition, dimensional analysis of the seismic signal recorded at PS10 makes it plausible that such nonlinear failure did occur beneath PS10. The high-frequency *S* waves that reached PS10 effectively interrogated the transient rheology of that region. We begin phenomenologically with observations from

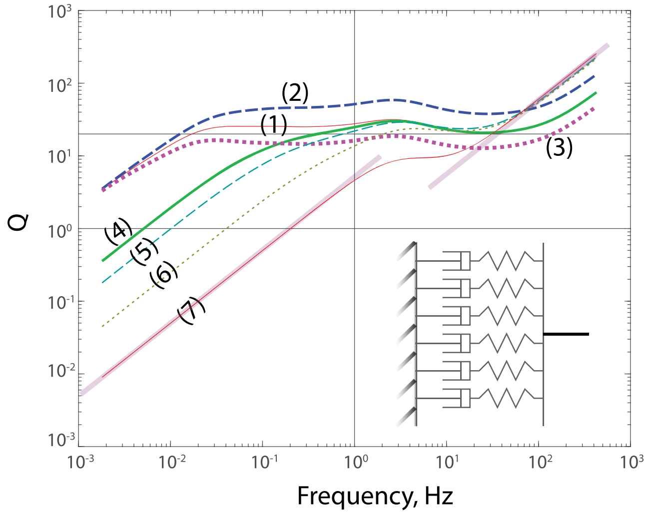

Figure 12. Quality factor Q plotted as a function of frequency for the seven models in Table 3. The models assume Maxwell elements of springs and dash pots acting in parallel to represent the equivalent instantaneous behavior of a heterogeneous rock mass. The curves approach viscous flow at low frequencies and linear elasticity at high frequencies. The parameters are calibrated to obtain relatively constant Q in the few tenths to few tens of Hertz range of interest. The curves shift to the right and retain their shapes when the viscosity of all the elements is increased by a uniform factor.

PS10 during the Denali mainshock and LUC during the Landers mainshock that should be explained. We then illustrate some attributes of applicable rheologies.

First, it is well known that the high-frequency S-wave signal recorded at PS10 was weak. In more detail, we found that these high-frequency waves apparently attenuated exponentially with frequency in Figure 6b. The high-frequency oscillations were weak ~0.1 g and had isotropic orientations in Figure 4. Some high-frequency signal was recorded at PS10 before the arrival of the near-field pulse and well after the pulse. These observations hint that the Denali fault could generate high-frequency S waves and that these waves could propagate to PS10. However, high-frequency signal remained weak in Figure 8 well after the near-field velocity pulse had passed. A simple relationship between instantaneous failure from the near-field velocity pulse and suppression of high-frequency S waves is thus not attractive. That is, the near-field velocity pulse may have damaged the crystalline rock beneath PS10, and the high-frequency S waves nonlinearly interacted with inelastic strain related to healing of this damage. Second with regard to LUC, high-frequency S waves briefly had low amplitudes during the near-field velocity pulse. Unlike PS10, stronger high-frequency S waves arrived both before and after this time. A simple relationship between instantaneous failure from the near-field velocity pulse and suppression of high-frequency S waves may be applicable. We note that granite underlies LUC (Sleep, 2012), while schists underlie PS10 (Carver et al., 2003) but do not attempt to extrapolate from this information. As with PS10, the weak high-frequency signal at LUC had isotropic orientation.

We continue with the observation from PS10 in Figure 6b that the horizontal spectra decay exponentially with frequency. That is, $Q(\omega)$ in (12) is crudely independent of frequency. This independence of frequency is commonly observed with ordinary linear attenuation of seismic waves within rock; mathematical formulations for exactly constant and nearly constant $Q(\omega)$ have been developed (e.g., Delépine et al., 2009; Emmerich & Korn, 1987; Kjartansson, 1979; Strick & Mainardi, 1982). Suitable arrangements of springs and dashpots can represent these rheologies.

We follow Delépine et al. (2009) by using springs and dashpots to represent complicated three-dimensional behavior within a heterogeneous rock mass. That is, we seek an equivalent medium for the rock mass. We stick to scalars for brevity. A full model that represented the elastic and inelastic behavior of each crack and the surrounding more intact rock is not particularly tractable.

We continue with the pseudolinear relationship of high-frequency inelastic strain to the high-frequency dynamic stress in (4). Representing a nonlinear process by a sequence of pseudolinear processes is clearly an approximation. Each segment s of a raypath instantaneously has an apparent (or differential) viscosity $\eta(s)$ and a shear modulus $G(s)$. That is, we apply an instantaneous Maxwell rheology that represents the well-known behavior of linear viscosity interacting in parallel with linear elasticity (Figure 12). The characteristic frequency of a spring is represented by the shear modulus

$$\omega(s) \equiv G(s)/\eta_{\text{app}}(s), \tag{14}$$

while the dash pot represents the apparent viscosity $\eta_{\text{app}}(s)$. The quality factor in (12) for each segment is frequency dependent, $Q(s) = \omega/\omega(s)$. In general, the amplitude change over one segment s is given by:

$$A(\omega, s) = A(\omega, s{-}1)\exp\left[\frac{-\omega t(s) Q^{-1}(s,\omega)}{2}\right], \tag{15}$$

where $A(\omega, s-1)$ is the amplitude at the end of segment $s-1$, $A(\omega, s)$ is the amplitude at the end of segment , and it takes the ray time t_s to cross the segment. Then using $Q^{-1} = \omega(s)/\omega$, we obtain the net diminution of energy over the full path:

$$A(\omega, s = s_{\max}) = A(\omega, 0)\prod_{s}^{s_{\max}} \exp\left[\frac{-t(s)\omega(s)}{2}\right] = A(\omega, 0)\exp\left[\frac{-\sum t(s)\omega(s)}{2}\right]. \tag{16}$$

The predicted diminution of amplitude is independent of frequency rather than exponentially dependent on frequency as in Figure 6b. The predicted amplitude of a sum of S waves arriving on various paths is also independent of frequency. These results indicate that heterogeneity along raypaths and nonlinear rheology in (4) do not directly explain the apparent exponent decrease of spectral amplitude with frequency in Figure 6b.

Continuing to follow Delépine et al. (2009), we allow multiple Maxwell elements to act in parallel (Figure 12). That is, we simply represent the more complicated situation where heterogeneous inelastic cracks and elasticity of the rock approximately act in parallel on the scale of the quarter wavelength of the high-frequency S waves. The instantaneous and local apparent value of Q^{-1} is

$$Q^{-1}(\omega) = \frac{\sum_{l=1} \frac{y(l)(\omega/\omega(l))}{1 + (\omega/\omega(l))^2}}{\sum_{l=1} \frac{y(l)(\omega/\omega(l))^2}{1 + (\omega/\omega(l))^2}}, \tag{17}$$

where l springs and dash pots act in parallel with characteristic frequencies of $\omega(l) \equiv G(l)/\eta_{\mathrm{app}}(l)$. The weighting coefficients $y(l)$ indicate the relative importance of each Maxwell element at the high-frequency limit $\omega \rightarrow \infty$, where no elastic strain occurs. These coefficients can sum to 1 without loss of generality. Equation (17), unlike equation (6) of Delépine et al. (2009), has no spring element acting in parallel with the Maxwell elements. Intuitively, the rheology should predict static nonlinear inelastic deformation associated with the shallow slip deficit (Kaneko & Fialko, 2011; Roten, Olsen, & Day, 2017) and thus reduce to instantaneous apparent viscosity at the limit of $\omega \rightarrow 0$. The expression $y(l)/\omega(l)$ indicates the relative importance of the elements at this limit.

For reference, the complex frequency-dependent shear modulus from the work of Delépine et al. (2009) is

$$G(\omega) = G_U\left[1 - \frac{\sum_{l} \frac{y(l)\omega(l)}{i\omega + \omega(l)}}{\sum_{l} y(l)}\right], \tag{18}$$

where G_U is the shear modulus at infinite frequency where the equation reduces to linear elasticity. The complex term indicates that the effective phase and group velocities are dispersive. We cannot make practical use of this effect as we have very little information on the exact times and places that the fault plane generated high-frequency S waves.

To represent the horizontal spectra in Figure 6b, we need to obtain relatively constant Q^{-1} for a moderate range of frequency like from 0.5 to 20 Hz. Only a few parallel Maxwell elements with intermediate frequencies are needed, and no especial significance is assigned to the precise frequencies of these elements (e.g., Delépine et al., 2009; Emmerich & Korn, 1987). We provide some examples in Figure 12 and provide the parameters in Table 3. We make no attempt to tweak parameters to make $Q^{-1}(\omega)$ quite flat in the range of interest.

We instead discuss general features of the models. The lowest characteristic frequency of models 1, 2, and 3 is 0.0005 Hz, and the highest frequency is 100 Hz. The predicted value of $Q(\omega)$ is flat over a broad range of frequencies. The lowest-frequency term has over 99% of the low-frequency response $y(l)/\omega(l)$ in Table 3. We vary the value of $y(1)$ from 0.8636 in model 2 to 0.625 in model 3 keeping the relative values of the other $y(l)$ constant. The value of the relatively constant part of $Q(\omega)$ is higher for model 2 than model 3. We increase the lowest characteristic frequency $f(1)$ in models 4 through 7 and hence also reduce the number of elements. The frequency range of relatively constant $Q(\omega)$ decreases with increasing . Model 7 has only two elements with 0.2 and 10 Hz. It still provides a plateau of $Q(\omega)$ in the region of interest. The 0.2 Hz element accommodates 85% of the high-frequency response and 99.65% of the low-frequency response. That is, a starting simple

Table 3
Maxwell Element Models

Model	1	2	3	4	5	6	7
f(1)‡	0.0005	0.0005	0.0005	0.005	0.01	0.04	0.2
y(1)	0.76	0.8636	0.625	0.76	0.8172	0.844	0.85
y(1)/ω(1)†	0.9957	0.9978	0.9919	0.9771	0.9926	0.9929	0.9965
f(2) ‡	0.005	0.005	0.005	0.01	0.07	0.3	10
y(2)	0.03	0.17	0.0469	0.03	0.0323	0.0333	0.15
f(3) ‡	0.07	0.07	0.07	0.07	0.3	1	
y(3)	0.03	0.17	0.0469	0.03	0.0323	0.033	
f(4) ‡	0.3	0.3	0.3	0.3	1	10	
y(4)	0.03	0.17	0.0469	0.03	0.0323	0.0389	
f(5) ‡	1	1	1	1	10	30	
y(5)	0.03	0.17	0.0469	0.03	0.0376	0.05	
f(6) ‡	10	10	10	10	30		
y(6)	0.035	0.0199	0.0547	0.035	0.0484		
f(7) ‡	30	30	30	30			
y(7)	0.0425	0.0241	0.0664	0.0425			
f(8) ‡	100	100	100	100			
y(8)	0.0425	0.0241	0.0664	0.0425			

‡ Frequency in Hertz. † Normalized so $y(l)/\omega(l)$ sums to 1.

instantaneous Maxwell model with just one element representing long-period response needs to be tweaked slightly by adding a second element to obtain a range of relatively constant $Q(\omega)$.

The mathematics now could be made very complicated and very nonunique by invoking (15) to combine attenuation over many segments of the raypath and then by summing over many rays. This effort would provide little insight, given our limited data. Rather, we qualitatively consider the physics of how a rheology with multiple Maxwell elements in parallel might arise with real crystalline rock.

We begin with LUC and assume for now that the nonlinear attenuation of high-frequency *S* waves is directly related to low-frequency nonlinear inelastic deformation in (5). We associate the low-frequency leading element $\omega(1) \equiv G(1)/\eta_{\mathrm{app}}(1)$ in (17) the apparent viscosity associated with the gross low-frequency deformation of the rock mass in (4). We associate the other elements with stress concentrations that act in parallel with the gross deformation on the length scale of the high-frequency waves. That is, high-frequency parallel elements $\omega(l) \equiv G(l)/\eta_{\mathrm{app}}(l)$ arise at stress concentrations with stiff elastic moduli and more importantly low apparent viscosities associated with high local stresses in a nonlinear material.

For LUC, we now need to qualitatively explain why strong high-frequency signal resumed once the near-field velocity pulse and its high dynamic stresses have passed. The models of Roten, Olsen, Cui, and Day (2017) indicate that nonlinearity beneath LUC is plausible during the near-field velocity pulse. A simple formation assumes that the values of the apparent viscosity of the elements are proportional to those of the low-frequency element associated with gross deformation $\eta_{\mathrm{app}}(l) \propto \eta_{\mathrm{app}}(1)$. The apparent viscosity $\eta_{\mathrm{app}}(1)$ in a nonlinear material increases in (3) when dynamic stresses wain and by this assumption the apparent viscosities of the other nonlinear elements. The effect in Figure 12 is to shift the curves to the left while retaining their shape. For example, increasing the viscosities in model 7 by a factor of 20 moves the strong attenuation out of the region of interest for high-frequency *S* waves and the material approaches linear elasticity in that range. The strain rate associated with gross deformation is then quite small. For reference, it would take a much larger increase in viscosity to shift model 2 enough to the left to suppress attenuation of high-frequency *S* waves.

In contrast, high-frequency *S* waves continued to be weak at PS10 well after the near-field velocity pulse had passed. A qualitative possibility is that the near-field velocity pulse damaged the crystalline rock. Classically, healing of damage that had reduced elastic constants progresses with the logarithm of time. Thus, rapid healing beneath PS10 in the immediate aftermath of the near-field pulse is plausible. The anelastic strain associated with this healing then acted nonlinearly with the high-frequency *S* waves, causing nonlinear attenuation. The healing of damage likely involves inelastic deformation at many stress concentrations. We attempted unsuccessfully to detect such healing within the uppermost crystalline rocks, beginning 7 days after the mainshock in section 6. We do not have data to look for immediate healing beneath PS10 and LUC.

8. Conclusions

Generic three-dimensional numerical calculations indicate that the near-field velocity pulse of strong earthquakes likely causes near-fault nonlinear failure (Roten et al., 2014, 2016, Roten, Olsen, Cui, & Day, 2017; Wang et al., 2019). In this case, dynamic stresses at depth scale with particle velocity and approximately with PGV is measured at the surface. Numerical models indicated that near-fault failure within crystalline rocks occurred during the near-field velocity pulse of the 1992 Landers earthquake (Roten et al., 2017). Horizontal PGV was 1.5 m s^{-1} at LUC 1.25 km from the fault. We thus suspect that nonlinear failure also occurred within crystalline rock beneath station PS10, which was ~3 km from the fault with PGA of 1.8 m s^{-1}, during the 2002 Denali earthquake. Our dimensional analysis of dynamic stresses during this event indicates that the near-field velocity pulse may have caused nonlinear failure down to ~ 2 km depth and that the uppermost crystalline rocks at ~100 m depth were most prone to failure. We unsuccessfully used aftershock data to look for healing of this shallow damage in section 6.

We concentrated on high-frequency *S* waves at PS10 and LUC that plausibly traversed crystalline rock, while low-frequency nonlinear attenuation from the near-field velocity pulse was occurring. In the immediate aftermath of the near-field pulse, high-frequency *S* waves plausibly traversed damaged crystalline rock. We recognize that both of these stations were isolated at the time of the earthquakes and not up to modern standards. In particular, these stations were triggered in a manner where they did not record any aftershocks. It is our intent to examine features that may become more evident in records of future well-recorded events. We do not claim definitive conclusions about nonlinear behavior of crystalline rock beneath PS10 and LUC.

To begin, shallow nonlinear attenuation likely occurred within the ~100 m thick layer of gravel beneath PS10, which complicates searching for nonlinear effects in the underlying crystalline rock. Scaling relationships for vertically ascending *S* waves provide insight. Dynamic stresses scale with the dynamic acceleration near the free surface; the normalized horizontal acceleration is the Coulomb ratio of horizontal shear traction to lithostatic stress. A prediction is that the normalized acceleration clips at the effective coefficient of friction. The resolved acceleration approached PGA during a circularly polarized third-cycle that was kinematically associated with the velocity pulse (Figure 4). During that time, the normalized acceleration did not exceed ~0.35, implying a reasonable effective coefficient of friction ~0.35. We marginally resolved that seismic velocities decreased in the gravel from damage associated with Coulomb failure and subsequent velocity increased from healing.

Other observations at PS10 cannot readily be associated with nonlinear Coulomb failure within the gravel: The normalized horizontal acceleration of high-frequency *S* waves at was weak, 0.1 g. The spectral amplitude of *S* waves decayed exponentially with frequency with a low and constant apparent *Q* for ~20 in Figure 6b. The horizontal acceleration of high-frequency *S* waves continued to be weak after the near-field velocity pulse had passed. Station LUC sat on crystalline rock. The normalized horizontal acceleration of high-frequency *S* waves was 0.2 g, somewhat more than at PS10. The high-frequency waves were only briefly weak, while the near-field velocity pulse passed.

We examined the physics of high-frequency *S* waves passing through the near-field velocity pulse with regard to these observations in section 7. The apparently constant *Q* at PS10 is not expected from a simple plastic or nonlinear Maxwell rheology for the crystalline rock, which does not preferentially suppress high frequencies. In section 7, we presented the well-known result that multiple Maxwell elements acting in parallel can produce apparently constant *Q* over the frequency range of interest. These elements represent nonlinear domains within a heterogeneous rock mass that have different instantaneous apparent viscosities.

The existence of numerous nonlinear inelastic domains might be associated with gross dynamic stresses and failure associated with the near-field velocity pulse. This situation might be applicable beneath LUC where weak high-frequency *S* waves impinged briefly during the near-field velocity pulse. However, weak high-frequency *S* waves continued to impinge on PS10 after the near-field velocity pulse had passed. A plausible rheology involves inelastic failure within the crystalline rock during the near-field velocity pulse. The high-frequency *S* waves then would interact nonlinearly with stress concentrations associated with healing of the damage.

Numerical models thus might resolve heterogeneous nonlinear material on the quarter-wavelength scale (~50 m) of the high-frequency waves. Alternatively, generic numerical models could constrain an equivalent material theory for high-frequency waves interacting with low-frequency stresses and damage in the crystalline rock. Then one could in principle calculate a low-frequency nonlinear model of the near-field pulse (Roten, Olsen, Cui, & Day, 2017) and then trace high-frequency waves through the nonlinear material. Numerical methods that selectively enhance numerical resolution in the region of interest might be applicable (Bielak et al., 2003; Yoshimura et al., 2003). All these approaches seem daunting.

With regard to societal issues, nonlinear suppression of *S* waves by the near-field velocity pulse may spare some near-fault structures from strong high-frequency shaking, like the small shed covering PS10. Still, high-frequency body waves impinge on near-fault sites. For example, high-frequency *S* and *P* waves both reached ~0.8 g at Lucerne in 1992 Landers earthquake, although the near-field velocity pulse may have briefly suppressed *S* waves at other times.

A new site effect is that damage to the uppermost crystalline rocks may have reduced their seismic velocities and thereby reduced the reflection coefficients between gravel and crystalline rock beneath PS10. Resonances putatively associated with the base of the gravel were weak following the near-field velocity pulse. We marginally resolved that these resonances returned ~15 s later. We attempted unsuccessfully to detect healing of the crystalline rock with aftershock data from temporary stations.

Appendix A.: Nonlinear Vertical *S*-wave model

We calculate synthetic surface seismograms to illustrate the effects of nearly plastic rheology. Our numerical method follows those of Sleep and Erickson (2014) and Sleep and Nakata (2015, 2017). Our objective is to present a generic model with upcoming waves and geological structure similar to those beneath PS10. We do not attempt to impose precise geological structure and to obtain full wiggle matches.

For simplicity, we numerically represented the PS10 structure with a layer over a half-space. The (uppermost) layer has an *S*-wave velocity of 400 m s^{-1} and is 110.25 m thick to fit on the numerical grid. The half-space has the *S*-wave velocity of 800 m s^{-1} to represent the reflection coefficient at its top in Figure 2. Density is 2.25 kg m^{-3}, which is constant with depth and time for numerical convenience.

We apply a staggered-grid method to represent ground motions, elastic strains, and inelastic strains from vertical *S* waves in two horizontal dimensions. The method is essentially finite difference with some aspects of finite elements over depth intervals. The shear traction, elastic strain, and inelastic strain nodes are evaluated at nodes at the center of elements. The shear modulus, the inelastic rheology, the shear wave velocity β, and the effective pressure are constant within these elements. The shear modulus and the inelastic rheology vary with depth between elements. We evaluate the time history (in steps of Δt) of these parameters. The depth range of elements is $\Delta Z = \beta \Delta t$, 0.5 m in the upper layer. For simplicity, no damage occurs so that the *S*-wave velocity and shear modulus do not change with time.

Displacement, velocity, acceleration, and the density for the momentum equation (5) are evaluated at intermediate nodes at the boundaries of the strain elements. The shear traction and inelastic strain are zero at the free surface, the location of the shallowest strain node. The surface acceleration is hence evaluated at the very shallow depth of $\beta \Delta t/2$, 0.25 m in the models.

At the start of the time step at time t_0, the program knows displacement at the spatial grids $U_i\{t_0\}$ and the displacement field at the previous time step $U_i\{t_0 - \Delta t\}$, where curly brackets indicate time steps and i indicates a horizontal direction. The difference between these quantities is the velocity a half step before t_0; $V_i\{t_0 - \Delta t/2\} = (U_i\{t_0\} - U_i\{t_0 - \Delta t\})/\Delta t$. The code finds the new velocity at a half time step ahead from the acceleration at each grid point at time step t_0, $V_i\{t_0+\Delta t/2\} = V_i\{t_0 - \Delta t/2\}+A_i\{t_0\}\Delta t$. The new displacement at $t_0+\Delta t$ is $U_i\{t_0+\Delta t\} = U_i\{t_0\}+V_i\{t_0+\Delta t/2\}\Delta t$.

We illustrate spatial derivatives using an example group of adjacent displacement nodes (up (U), center (C), and down (D)). The objective is to find the acceleration at time t_0. The shear traction in the i direction between two nodes (down and center) is

$$\tau_i(\mathrm{D},\mathrm{C})_{\{t_0\}} = G_\mathrm{D}\left[\frac{U_{\mathrm{D},i} - U_{\mathrm{C},i}}{\Delta Z}\right]_{\{t_0\}} - G_\mathrm{D}\varepsilon_i(\mathrm{D},\mathrm{C})_{\{t_0\}}, \tag{A1}$$

where G_D is the shear modulus in the lower element, the first term represents total strain, and ε_i(D,C) is inelastic engineering strain. The acceleration of the center node from (5) is

$$A_i = \frac{1}{\rho}\left[\frac{\tau_i(\mathrm{D},\mathrm{C}) - \tau_i(\mathrm{C},\mathrm{U})}{\Delta Z}\right]_{\{t_0\}}. \tag{A2}$$

The shear modulus G and inelastic strain ε in general depend on the current stress and history of the rock.

Equation (A1) implies an inelastic strain rate at each node where failure occurs, which is within the uppermost layer in our models; the half-space is elastic. One requires that the rate of inelastic strain in (A1) be consistent with computed stress. Formally for each horizontal direction i:

10.1029/2019JB018386

$$\tau_i\{t_0\} = G_D\left[\frac{U_{D,i} - U_{C,i}}{\Delta Z}\right]_{\{t_0\}} - G_D\varepsilon_i\{t_0 - \Delta t\} - G_D\left[\frac{\tau_i\{t_0\}}{|\tau\{t_0\}|}\right]\Delta\varepsilon(|\tau\{t_0\}|), \tag{A3}$$

where $\Delta\varepsilon(|\tau\{t_0\}|)$ is the resolved inelastic strain during the time step and the expression is general and does not imply any specific rheology. The bracket in the third term causes the horizontal inelastic strain rate to have the orientation of the shear traction as in (3). The shear traction (as τ_i and $|\tau\{t_0\}|$) appears on both sides of (A3). The equation is readily solved by iteration if the inelastic strain rate increases smoothly and monotonically with stress. We let the inelastic strain per time step Δt function in the i direction be

$$\Delta\varepsilon_i = \varepsilon_i'\Delta t = \zeta\left[\frac{\tau_i\{t_0\}}{|\tau\{t_0\}|}\right]\left[\frac{\tau_M}{G}\right]\left[\frac{|\tau\{t_0\}| - \tau_B}{\tau_M}\right]^m, \tag{A4}$$

where inelastic strain has the sign to relieve stress, $\tau_M = \rho g \mu_M z$ is a stress where frictional creep becomes fast at the Coulomb stress ratio μ_M, $\tau_B = \rho g \mu_B z$ implies that no inelastic strain occurs below a Bingham coefficient of friction of μ_B ($\varepsilon' = 0$; $|\tau| \leq \tau_B$), and m is an exponent that represents transition between slow and fast deformation as dynamic stress increases. The dimensionless constant ζ calibrates (A4) so that rapid strain rates begin at the desired shear traction. That is, we adjust the constant ζ to obtain the desired transition stress between very slow and very fast creep at a Coulomb ratio of ~0.35. Equation (A4) becomes ordinary power-law creep if $\tau_B = 0$; we keep τ_B at a finite value so that weak shaking is linear. Equation (A4) approaches a plastic yield surface in the limit of large m. There are only two qualitative free parameters: The shear traction where failure starts and the shear traction where the strain rate becomes so high that larger shear tractions are precluded. Our model parameters provide a rapid increase of strain rate with shear traction. We do not impose nearly pure plasticity so that loops in Figure 3b are visible. Our parameters are $m = 5$; μ_M is 0.3; μ_B is 0.4; ζ is 200 to yield an effective coefficient of friction of ~0.35 in Figure 3, as observed in Figure 4.

The initial conditions represent quiescence before seismic waves impinge. The inelastic strains, displacements, velocities, and accelerations are all zero. We place the bottom node very deep at 20,000 grid spacings. We stop the calculation before the surface-reflected wave impinges on the artificial basal boundary and ascends back to the shallow region of interest. We start the upcoming wave by imposing displacements on the bottom node. We combine displacements of the form $D_i = D_{0,i}(1 - \cos(\omega t))$ to obtain a circularly polarized low-frequency signal and an east-west high-frequency signal. We adjust the displacement factors $D_{0,i}$ to obtain the desired peak accelerations for the low-frequency components and high-frequency components of the signal. The displacement and velocity are zero and continuous at the starting time $t = 0$. The acceleration jumps to its peak value when the signal begins. We window Figure 3 in the time of interest when the impinging signal is circularly polarized.

Acknowledgments

This research was supported by the Southern California Earthquake Center. SCEC is funded by NSF Cooperative Agreement EAR-0106924 and USGS Cooperative Agreement 02HQAG0008. The SCEC contribution number for this paper is 9959. We thank William Ellsworth for providing digital records for the Denali mainshock. He and Eric Dunham answered numerous questions. Y. Kaneko and five anonymous reviewers provided helpful comments. Natalia Ruppert, Michael West, William Ellsworth, Arthur Frankel, Amelia Redhill, and Alena Leeds helped in locating the missing aftershock data. Denali mainshock data are from the work of Ellsworth et al. (2004) and are available from Cosmos Database URL (https://strongmotioncenter.org/vdc/scripts/event.plx?evt=814#3037). Data from the Landers mainshock are from the works of Chen (1995) and Iwan and Chen (1995). They are available from Cosmos Database (https://strongmotioncenter.org/vdc/scripts/event.plx?evt=18). Denali aftershock data are available by request from the USGS in Golden Colorado. All other general data are within cited publications. The computer program used to generate Figure 3 is available from the Stanford Digital Repository website (https://purl.stanford.edu/ws581hq4747).

References

Afacan, K. B., Brandenberg, S. J., & Stewart, J. P. (2014). Centrifuge modeling studies of site response in soft clay over wide strain range [ASCE]. *J Geotech Geoenviron Eng*, *140*(2), 04013003.

Andrews, D. J. (2004). Rupture models with dynamically determined breakdown displacement. *Bulletin of the Seismological Society of America*, *94*(3), 769–775.

Andrews, D. J. (2005). Rupture dynamics with energy loss outside the slip zone. *Journal of Geophysical Research*, *110*, B01307. https://doi.org/10.1029/2004JB003191

Anooshehpoor, A., & Brune, J. N. (1989). Foam rubber modelling of the topographic and dam interaction effects at Pacoima Dam. *Bulletin of the Seismological Society of America*, *79*(5), 1347–1360.

Aoi, S., Kunugi, T., & Fujiwara, H. (2008). Trampoline effect in extreme ground motions. *Science*, *332*, 727–730.

Asano, K., Iwata, T., & Irikura, K. (2005). Estimation of source rupture processes and strong ground motion simulation of the Denali, Alaska. *Earthquake Bulletin of the Seismological Society of America*, *95*, 1701–1715. https://doi.org/10.1785/0120040154

Assimaki, D., Li, W., Steidl, J. H., & Schmedes, J. (2008). Quantifying nonlinearity susceptibility via site-response modeling uncertainty at three sites in the Los Angeles Basin. *Bulletin of the Seismological Society of America*, *98*(5), 2364–2390.

Baker, J. W. (2007). Quantitative classification of near-fault ground motionsusing wavelet analysis. *Bulletin of the Seismological Society of America*, *97*(5), 1486–1501.

Ben Zion, Y., & Lyakhovsky, V. (2019). Representation of seismic sources sustaining changes of elastic moduli. *Geophysical Journal International*, *217*, 135–139.

Bielak, J., Loukakis, K., Hisada, Y., & Yoshimura, C. (2003). Domain reduction method for three-dimensional earthquake modeling in localized regions, Part I: Theory. *Bulletin of the Seismological Society of America*, *93*(2), 817–824.

Bonilla, L. F., Guéguen, P., & Ben-Zion, Y. (2019). Monitoring coseismic changes of shallow material during strong ground motion with interferometry and autocorrelation. *Bulletin of the Seismological Society of America*, *109*, 187–198.

Bradley, B. A., & Cubrinovski, M. (2011). Near-source ground motions observed in the 22 February 2011 Christchurch earthquake. *Seismological Research Letters*, *82*(6), 853–865.

Brocher, T. M., Fuis, G. S., Lutter, W. J., & Christensen, N. I. (2004). Seismic velocity models for the Denali fault zone along the Richardson Highway, Alaska. *Bulletin of the Seismological Society of America*, *94*(6B), S85–S106.

Carpenter, N. S., Wang, Z., Woolery, E. W., & Rong, M. (2018). Estimating site response with recordings from deep boreholes and HVSR: Examples from the Mississippi embayment of the Central United States. *Bulletin of the Seismological Society of America*, *108*(3A), 1199–1209. https://doi.org/10.1785/0120170156

Carver, D., T. Plucinski, A. Frankel, and E. Safak (2003) Data report of aftershocks of the 03 November 2002, Mw 7.9, Denali Fault earthquake recorded near the fault rupture at the Richardson Highway and Alyeska Pipeline. U.S. Geological Survey Open-File Report 03-158. https://pubs.usgs.gov/of/2003/ofr-03-158/OFR-03-158.html

Cattania, C., Hainzl, S., Wang, L., Enescu, B., & Roth, F. (2015). Aftershock triggering by postseismic stresses: A study based on Coulomb rate-and-state models. *Journal of Geophysical Research: Solid Earth*, *120*, 2388–2407. https://doi.org/10.1002/2014JB011500

Chen, X. (1995) Near-field ground motion from the Landers Earthquake. PhD thesis California Institute of Technology, 147 pp.

Cocco, M., Tinti, E., Marone, C., & Piatanesi, A. (2009). Scaling of slip weakening distance with final slip during dynamic earthquake rupture. In E. Fukuyama (Ed.), *fault-zone properties and earthquake rupture dynamics*, *International Geophysics Series*, (Vol. 94, pp. 163–186). Amsterdam: Elsevier.

Delépine, N., Lenti, L., Bonnet, G., & Semblat, J.-F. (2009). Nonlinear viscoelastic wave propagation: an extension of nearly constant Attenuation models. *Journal of Engineering Mechanics (ASCE)*, *135*(11), 1305–1314. https://doi.org/10.1061/(ASCE)0733-9399(2009)135:11(1305) >. <hal-00409783v2>

Dreger, D. S., Oglesby, D. D., Harris, R., Ratchkovski, N., & Hansen, R. (2004). Kinematic and dynamic rupture models of the November 3, 200 Mw7.9 Denali, Alaska, earthquake. *Geophys. Res. Lett.*, *31*, L04605. https://doi.org/10.1029/2003GL018333

Drucker, D. C., & Prager, W. (1952). Soil mechanics and plastic analysis for limit design. *Quarterly of Applied Mathematics*, *10*, 157–165.

Dunham, E. M., & Archuleta, R. J. (2004). Evidence for a supershear transient during the 2002 Denali Fault earthquake. *Bulletin of the Seismological Society of America*, *94*(6B), S256–S268. https://doi.org/10.1785/0120040616

Eberhart-Phillips, D., & 28 coauthors (2003). The 2002 Denali fault earthquake. *Alaska: A large-magnitude, slip-partitioned event, Science*, *300*, 1113–1118.

Ellsworth, W. L., Çelebi, M., Evans, J. R., Jensen, E. G., Kayen, R., Metz, M. C., et al. (2004). Near-field ground motion of the 2002, Denali Fault, Alaska, earthquake recorded at Pump Station 10. *Earthquake Spectra*, *20*(3), 597–615.

Emmerich, H., & Korn, M. (1987). Incorporation of attenuation into time-domain computations of seismic wave fields. *Geophysics*, *52*(9), 1252–1264.

Evans, J. R., E. G. Jensen, R. Sell, C. D. Stephens, D. J. Nyman, R. C. Hamilton, and W. C. Hager (2006) Calibration of PS09, PS10, and PS11 Trans-Alaska Pipeline System strong-motion instruments, with acceleration, velocity, and displacement records of the Denali Fault earthquake, 03 November 2002. Open-File Report 2006–1028, U. S. Geological Survey, Menlo Park CA, 54 pp.

Fischer, A. D., Peng, Z. G., & Sammis, C. G. (2008). Dynamic triggering of high- frequency bursts by strong motions during the 2004 Parkfield earthquake sequence. *Geophysical Research Letters*, *35*, L12305. https://doi.org/10.1029/2008GL033905

Fischer, A. D., & Sammis, C. G. (2009). Dynamic driving of small shallow events during strong motion. *Bulletin of the Seismological Society of America*, *99*, 1720–1729.

Fischer, A. D., Sammis, C. G., Chen, Y. L., & Teng, T.-L. (2008). Dynamic triggering by strong motion P- and S-waves: Evidence from 1999 Chi-Chi, Taiwan earthquake. *Bulletin of the Seismological Society of America*, *98*, 580–592.

Frankel, A. (2004). Rupture process of the M 7.9 Denali Fault, Alaska, earthquake: Subevents, directivity, and scaling of high-frequency ground motions. *Bulletin of the Seismological Society of America*, *94*, S234–S255.

Ghofrani, H., Atkinson, G. M., & Goda, K. (2013). Implications of the 2011 M9.0 Tohoku Japan earthquake for the treatment of site effects in large earthquakes. *Bulletin of Earthquake Engineering*, *11*, 171–203.

Goto, H., Kaneko, Y., Young, J., Avery, H., & Damiano, L. (2019). Extreme accelerations during earthquakes caused by elastic flapping effect. *Scientific Reports*, *9*, 1117.

Goto, H., Sawada, S., & Hirai, T. (2011). Conserved quantity of elastic waves in multi-layered media: 2D. *SH case, normalized energy density, wave motion*, *48*(7), 603–613.

Graves, R., & Pitarka, A. (2016). Kinematic ground-motion simulations on rough faults including effects of 3D stochastic velocity perturbations. *Bulletin of the Seismological Society of America*, *106*(5), 2136–2153.

Güler, E., & Afacan, K. B. (2019). Effect of Frequency on the dynamic properties of sand. Eskişehir Technical University. *Journal of Science and Technology A Applied Sciences and Engineering*, *20*(1), 70–79. https://doi.org/10.18038/aubtda.459191

Haeussler, P. J., Schwartz, D., Dawson, T., Stenner, H., Lienkaemper, J., Sherrod, B., et al. (2004). Surface rupture and slip distribution of the Denali and Totschunda faults in the 3 November 2002 M 7.9 earthquake, Alaska. *Bulletin of the Seismological Society of America*, *94*, S23–S52. https://doi.org/10.1785/0120040626

Han, B., Yang, Z., Zdravković, L., & Kontoe, S. (2015). Non-linearity of gravelly soils under seismic compressional deformation based on KiK-net downhole array observations. *Géotechnique Letters*, *5*, 287–293. https://doi.org/10.1680/jgele.15.00130

Hassani, B., & Atkinson, G. M. (2018). Adjustable generic ground-motion prediction equation based on equivalent point-source simulations: Accounting for kappa effects. *Bulletin of the Seismological Society of America*, *108*(2), 913–928.

Hill, R., & Orowan, E. (1948). A theory of the yielding and plastic flow of anisotropic metals. *Proceedings of the Royal Society of London A*, *193*, 283–297.

Hreinsdottir, S., Freymueller, J. T., Fletcher, H. J., Larsen, C. F., & Bürgmann, R. (2003). Coseismic slip distribution of the 2002 MW7.9 Denali fault earthquake, Alaska, determined from GPS measurements. *Geophysical Research Letters*, *30*(13), 1670. https://doi.org/10.1029/2003GL017447

Iwan, W. D., & Chen, X. (1995). Important near-field ground motion data from the Landers earthquake. In G. Duma (Ed.), *10th European Conference on Earthquake Engineering* (pp. 229–234). Rotterdam: Balkema.

Jeffreys, H. (1961). Small corrections in the theory of surface waves. *Geophysical Journal of the Royal Astronomical Society*, *6*, 115–117. https://doi.org/10.1111/j.1365-246X.1961.tb02965.x

Kaneko, Y., & Fialko, Y. (2011). Shallow slip deficit due to large strike-slip earthquakes in dynamic rupture simulations with elasto-plastic off-fault response. *Geophysical Journal International*, *186*, 1389–1403. https://doi.org/10.1111/j.1365-246X.2011.05117.x

Kayen, R., Thompson, E., Minasian, D., Moss, R. E. S., Collins, B. D., Sitar, N., et al. (2004). Geotechnical reconnaissance of the 2002 Denali Fault, Alaska, Earthquake. *Earthquake Spectra*, *20*, 639–667.

Kinoshita, S. (2011). A stochastic approach for evaluating the nonlinear dynamics of vertical motion recorded at the IWTH25 site for the 2008M_w 6.9 Iwate–Miyagi Inland earthquake. *Bulletin of the Seismological Society of America*, *101*, 2955–2966.

Kjartansson, E. (1979). Constant Q wave propagation and attenuation. *Journal of Geophysical Research*, *84*, 4737–4748.

Liao, B.-Y., & Huang, H.-C. (2007). Rupture process of the 2002 M_w 7.9 Denali Earthquake, Alaska, using a newly devised hybrid deconvolution method. *Bulletin of the Seismological Society of America*, *98*, 162–179.

Lubliner, J. (1990). *Plasticity theory*, (p. 495). New York: Macmillan.

Ma, S., & Andrews, D. J. (2010). Inelastic off-fault response and three-dimensional dynamics of earthquake rupture on a strike-slip fault. *Journal of Geophysical Research*, *115*, B04304. https://doi.org/10.1029/2009JB006382

Martirosyan, A., Hansen, R., & Ratchkovski, N. (2004). Strong-motion records of the 2002 Denali Fault, Alaska, earthquake. *Earthquake Spectra: August 2004*, *20*(3), 579–596.

Menq, F.-Y. (2003) Dynamic properties of sandy and gravelly soils. PhD thesis. The University of Texas at Austin, 364 pp.

Nakata, N., & Snieder, R. (2011). Near-surface weakening in Japan after the 2011 Tohoku-Oki earthquake. *Geophysical Research Letters*, *38*, L17302. https://doi.org/10.1029/2011GL048800

Oglesby, D. D., Dreger, D. S., Harris, R. A., Ratchkovski, N., & Hansen, R. (2004). Inverse kinematic and forward dynamic models of the 2002 Denali fault earthquake, Alaska. *Bulletin of the Seismological Society of America*, *94*, S214–S233.

Paolucci, R., Gatti, F., Infantino, M., Ozcebe, A. G., Smerzini, C., & Stupazzini, M. (2018). Broad-band ground motions from 3D physics-based numerical simulations using Artificial Neural Networks. *Bulletin of the Seismological Society of America*, *108*, 1272–1286.

Roten, D., Cui, Y., Olsen, K., Day, S., Withers, K., Savran, W., et al. (2016). High-frequency nonlinear earthquake simulations on petascale heterogeneous supercomputers, paper presented at ACM/IEEE International Conference for High Performance Computing, Networking, Storage and Analysis (SC'16), pp. 957–968, IEEE Press, Salt Lake City, Utah, 13–18 Nov.

Roten, D., Olsen, K., Cui, Y., & Day, S. (2017). Quantification of fault zone plasticity effects with spontaneous rupture simulations, Pure Appl. *Geophysics*, *174*(9), 3369–3391. https://doi.org/10.1007/s00024-017-1466-5

Roten, D., Olsen, K. B., & Day, S. M. (2017). Off-fault deformations and shallow slip deficit from dynamic rupture simulations with fault zone plasticity. *Geophysical Research Letters*, *44*, 7733–7742. https://doi.org/10.1002/2017GL074323

Roten, D., Olsen, K. B., Day, S. M., Cui, Y., & Fäh, D. (2014). Expected seismic shaking in Los Angeles reduced by San Andreas fault zone plasticity. *Geophysical Research Letters*, *41*, 2769–2776. https://doi.org/10.1002/2014GL059411

Sleep, N. H. (2010). Strong seismic shaking of randomly pre-stressed brittle rocks, rock damage, and nonlinear attenuation. *Geochemistry, Geophysics, Geosystems*, *11*, Q10002. https://doi.org/10.1029/2010GC003229

Sleep, N. H. (2012). Site resonance from strong ground motions at Lucerne, California, during the 1992 Landers Mainshock. *Bulletin of the Seismological Society of America*, *102*(4), 1505–1513. https://doi.org/10.1785/0120110267

Sleep, N. H. (2016). Shallow sedimentary rock as a fragile geological feature: Effects of clay content and hydrology on frictional strength. *Bulletin of the Seismological Society of America*, *106*. https://doi.org/10.1785/0120150376

Sleep, N. H., & Nakata, N. (2015). Nonlinear attenuation from the interaction between different types of seismic waves and interaction of seismic waves with shallow ambient tectonic stress. *Geochemistry, Geophysics, Geosystems*, *16*, 2336–2363.

Sleep, N. H., & Nakata, N. (2017). Nonlinear attenuation of *S* waves by frictional failure at shallow depths. *Bulletin of the Seismological Society of America*, 1828–1848.

Strick, E., & Mainardi, F. (1982). On a general class of constant-*Q* solids. Geophys. *Journal of the Royal Astronomical Society*, *69*, 415–429.

Tao, K., Liu, T., Ning, J., & Niu, F. (2014). Estimating sedimentary and crustal structure using wavefield continuation: Theory, techniques and applications. *Geophysical Journal International*, *197*(1), 443–457.

Tinti, E., Bizzarri, A., Piatanesi, A., & Cocco, M. (2004). Estimates of slip weakening distance for different dynamic rupture models. *Geophysical Research Letters*, *31*, L02611. https://doi.org/10.1029/2003GL018811

Tobita, T., Iai, S., & Iwata, T. (2010). Numerical analysis of near-field asymmetric vertical motion. *Bulletin of the Seismological Society of America*, *100*(4), 1456–1469.

Turcotte, D. L., & Schubert, G. (2002). *Geodynamics*, (2nd ed.p. 456). Cambridge, UK: Cambridge University Press.

Wald, D. J., & Heaton, T. H. (1994). Spatial and temporal distribution of slip for the 1992 Landers, California, earthquake. *Bulletin of the Seismological Society of America*, *84*(3), 668–691.

Walker, K. T., & Shearer, P. M. (2009). Illuminating the near-sonic rupture velocities of the intracontinental Kokoxili Mw7.8 and Denali fault Mw 7.9 strike-slip earthquakes with global P wave back projection imaging. *J. Geophys. Res.*, *114*, B02304. https://doi.org/10.1029/2008JB005738

Wang, Y., Day, S. M., & Denolle, M. A. (2019). Geometric controls on pulse-like rupture in a dynamic model of the 2015 Gorkha earthquake. *Journal of Geophysical Research: Solid Earth*, *124*, 1544–1568.

Weertman, J., & Blacic, J. (1984). Harper-Dorn creep: An artifact of low-amplitude temperature cycling. *Geophysical Research Letters*, *11*, 117–120.

Wesson, R. L., & Boyd, O. S. (2007). Stress before and after the 2002 Denali fault earthquake. *Geophysical Research Letters*, *34*, L07303. https://doi.org/10.1029/2007GL029189

Wright, T. J., Lu, Z., & Wicks, C. (2004). Constraining the slip distribution and fault geometry of the MW 7.9, 3 November 2002, Denali Fault earthquake with Interferometric Synthetic Aperture Radar and Global Positioning System data. *Bulletin of the Seismological Society of America*, *94*, S175–S189.

Wu, C., & Peng, Z. (2011). Temporal changes of site response during the 2011 Mw 9.0 off the Pacific coast of Tohoku earthquake. *Earth, Planets and Space*, *63*, 791–795.

Yamada, M., Mori, J., & Heaton, T. (2009). The slapdown phase in high-acceleration records of large earthquakes. *Seismological Research Letters*, *80*(4), 559–564.

Yoshimura, C., Bielak, J., Hisada, Y., & Fernández, A. (2003). Domain reduction method for three-dimensional earthquake modeling in localized regions, Part II: Verification and applications. *Bulletin of the Seismological Society of America*, *93*(2), 825–840.